Journal of Sound and Vibration 560 (2023) 117787

Contents lists available at ScienceDirect

Journal of Sound and Vibration

journal homepage: www.elsevier.com/locate/jsvi

Modelling acoustic radiation from vibrating surfaces around coincidence: Radiation into fluids

Erlend Magnus Viggen [a,*], Håvard Kjellmo Arnestad [b]

[a] Centre for Innovative Ultrasound Solutions, Department of Circulation and Medical Imaging, Norwegian University of Science and Technology, Prinsesse Kristinas gt. 3, Trondheim, 7030, Norway
[b] Department of Informatics, University of Oslo, Gaustadalléen 23B, Oslo, 0316, Norway

ARTICLE INFO

Keywords:
Subsonic radiation
Surface vibrations
Inhomogeneous waves
Leaky guided waves
Lamb waves

ABSTRACT

It is well-known that vibrating surfaces generate sound waves in adjacent fluids. According to the classical radiation model, the nature of these waves depends on whether the vibration's phase speed c_v is above (*supersonic*) or below (*subsonic*) the fluid sound speed c_f. The transition between these two domains is known as *coincidence*. In the supersonic domain, the sound wave radiates into the fluid. In the subsonic domain, the classical model states that the wave becomes evanescent and clings to the surface. In the last 30 years, however, several articles on leaky guided waves have reported radiating waves in the subsonic domain, which is at odds with the classical model. In this article, we investigate an enhanced model for sound radiation near and below coincidence. Unlike the classical model, this model fully respects conservation of energy by balancing the radiated power with power lost from the guided wave underlying the vibration. The model takes into account that this power loss and the consequent attenuation of the surface vibration result in an *inhomogeneous* radiated sound wave — an effect that cannot be neglected near coincidence. We successfully validate the model against exact solutions for leaky A_0 Lamb waves around coincidence. The model can also be used as a perturbation method to predict the attenuation of leaky A_0 waves from the properties of free A_0 waves, giving more accurate estimates than existing perturbation methods. We further investigate subsonic leaky A_0 waves using the enhanced model. Thereby we, for example, explain the peculiar reappearance or persistence of the leaky A_0 wave at lower frequencies, an effect brought to attention by previous theoretical studies.

1. Introduction

Vibrations on the surface of structures such as blocks, plates, pipes, beams, or membranes can cause sound waves to radiate into adjacent fluids or solids. This very well-known phenomenon is crucial in many diverse fields of science and engineering, for example, building acoustics, microelectromechanical system design, and acoustic logging of petroleum wells.

It is widely held in textbooks and other scientific literature [1–8] that surface vibrations can only radiate sound waves into the fluid when the vibrational wave is *supersonic*, i.e., when its speed c_v exceeds the sound speed c_f of the fluid. In contrast, when the vibration is *subsonic*, i.e., slower than the sound speed, the sound wave is *evanescent*; it clings to the vibrating surface and does not radiate out into the fluid. In this article, we denote this as the *classical model* of sound radiation from vibrating surfaces. It can be found from a straightforward derivation which we will now briefly cover to facilitate discussing this model and its shortcomings.

* Corresponding author.
E-mail address: erlend.viggen@ntnu.no (E.M. Viggen).

https://doi.org/10.1016/j.jsv.2023.117787
Received 23 September 2022; Received in revised form 20 April 2023; Accepted 12 May 2023
Available online 16 May 2023

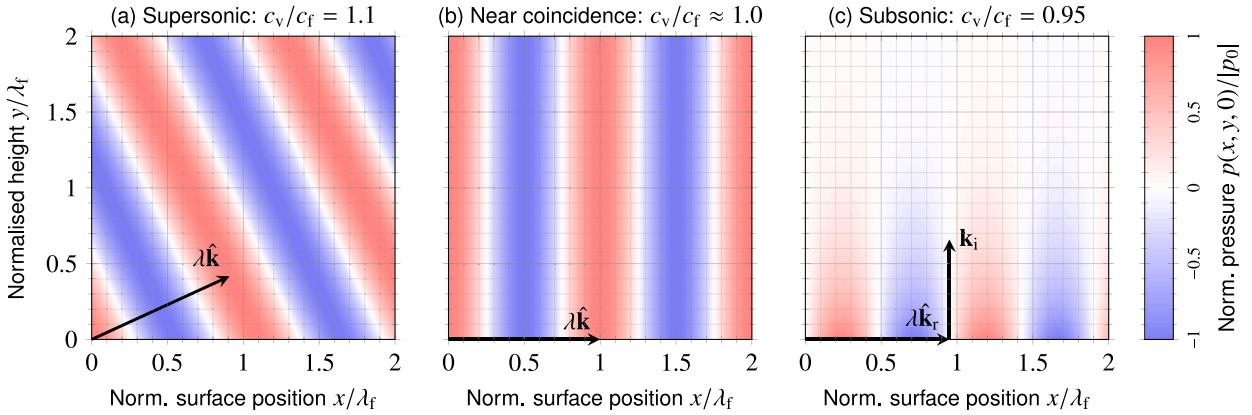

Fig. 1. Three pressure fields in the fluid above a surface at $y = 0$ that vibrates according to Eq. (2) at three different phase speeds $c_v = \omega/k_x$. Here, $\lambda_f = 2\pi/k$ is the wavelength of a homogeneous sound wave, and $\lambda = 2\pi/|\mathbf{k}_r|$ the actual wavelength of the plotted sound wave. Hats signify unit vectors, and $\mathbf{k}_r$ and $\mathbf{k}_i$ are the real and imaginary components of the wavevector $\mathbf{k}$, respectively.

Consider an infinite vibrating surface in the x–z plane, coupled to a semi-infinite fluid with sound speed c_f at $y \geq 0$. For a harmonic vibration propagating in the x direction, the normal velocity is

$$v_y(x, y = 0, t) = v_{y0}\, e^{i(k_x x - \omega t)}, \tag{1}$$

where $\omega = 2\pi f$ and f are real-valued angular and ordinary frequencies, respectively, k_x is the real-valued surface wavenumber, and v_{y0} is the velocity amplitude. (Here and onwards, we use subscripted zeroes to indicate various quantities' values at $x = y = 0$ and $t = 0$.) The vibration propagates with a phase speed $c_v = \omega/k_x$, and we assume the vibration to be weak enough that we can treat the problem linearly.

The vibration generates a sound wave in the fluid, whose pressure field we can express as a general harmonic plane wave in the x–y plane:

$$p(x, y, t) = p_0\, e^{i(k_x x + k_y y - \omega t)} = p_0\, e^{i(\mathbf{k}\cdot\mathbf{r} - \omega t)}. \tag{2}$$

Here, $\mathbf{k} = (k_x, k_y)$ is the wavevector and $\mathbf{r} = (x, y)$ is the coordinate vector. To satisfy the boundary conditions imposed by the vibrating surface, the pressure wave is related to the surface vibration through ω and k_x, and its amplitude p_0 is proportional to v_{y0}. (We defer the exact relation between p_0 and v_{y0} to Section 3.1.)

The relation between the wavevector components k_x and k_y in the fluid can be found by inserting Eq. (2) into the wave equation for lossless fluids:

$$\frac{1}{c_f^2}\frac{\partial^2 p}{\partial t^2} = \nabla^2 p \qquad \Longrightarrow \qquad \left(\frac{\omega}{c_f}\right)^2 = k_x^2 + k_y^2 = \mathbf{k}\cdot\mathbf{k} = k^2. \tag{3}$$

In a lossless fluid with a real-valued frequency ω of the surface vibration, the sound wavenumber $k = |\mathbf{k}| = \omega/c_f$ is also real-valued. For a given k and surface wavenumber k_x, this relation gives us

$$k_y = \pm k\sqrt{1 - \left(\frac{k_x}{k}\right)^2} = \pm k\sqrt{1 - \left(\frac{c_f}{c_v}\right)^2}. \tag{4}$$

Hence, this classical model of sound radiation from vibrating surfaces implies two domains with very different behaviour, as Fig. 1 shows:

Supersonic domain ($c_f < c_v$, Fig. 1a): Here, k_y is real-valued. Choosing the positive sign in Eq. (4) leads to an *outgoing* wave that propagates out from the vibrating surface, carrying energy away from the surface vibration into the fluid. The negative sign leads to an *incoming* wave that propagates into the vibrating surface, carrying energy into the surface vibration. In this work, we study the former case of outward radiating waves.

Subsonic domain ($c_v < c_f$, Fig. 1c): Here, $k_y = \pm ik\sqrt{(c_f/c_v)^2 - 1}$ is a purely imaginary number, and Eq. (2) becomes $p(x, y, t) = p_0\, e^{i(k_x x - \omega t)}\, e^{\mp yk\sqrt{(c_f/c_v)^2 - 1}}$. The positive sign of k_y describes an exponentially decaying *evanescent* wave, which propagates along the surface and carries no energy away into the fluid. The negative sign of k_y leads to a solution generally rejected by the sources that consider it [2,5,8], because it describes a wave that grows exponentially towards infinity with the distance to the surface.

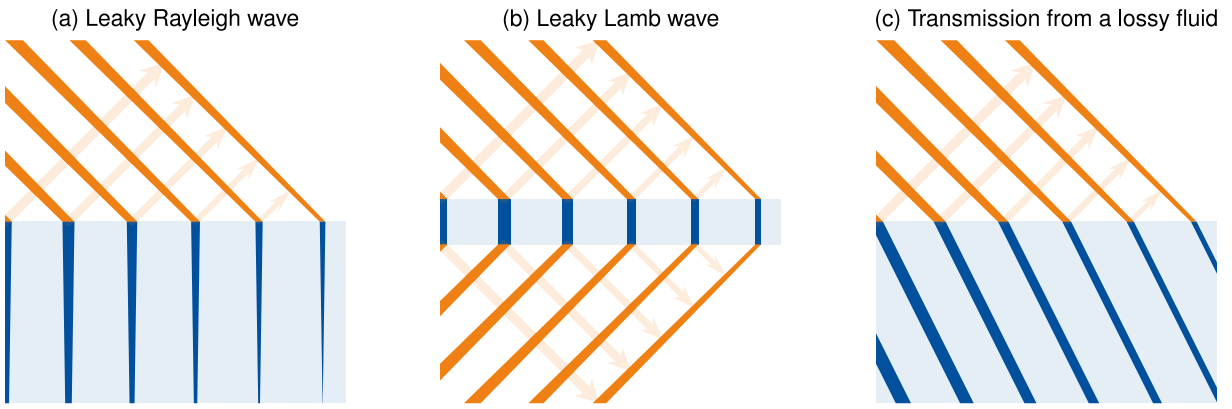

Fig. 2. Inhomogeneous plane waves (orange) in a lossless fluid (white) from three different origins, all of which can be modelled as attenuated surface vibrations. Thick solid lines represent wavefronts whose amplitudes are indicated by the line thickness. Semi-transparent arrows represent the characteristic lines along which the waves propagate. In any lossless fluid, the wavefront amplitude remains constant along these characteristic lines. (a) Leaky Rayleigh waves in a semi-infinite solid (blue). (b) Leaky Lamb waves in a solid plate (blue). (c) Attenuated plane waves in a lossy fluid (blue), transmitted to a lossless fluid; waves reflected from the fluid-fluid interface are not shown. (For interpretation of the references to colour in this figure legend, the reader is referred to the web version of this article.)

Between these two domains is the boundary of *coincidence* where $c_\mathrm{f} = c_\mathrm{v}$, i.e., where the vibrational phase speed *coincides* with the fluid speed of sound. Near coincidence, the sound wave propagates nearly parallel to the surface, as we can see from Fig. 1b. (Exactly at coincidence, however, the pressure wave amplitude p_0 has an infinite discontinuity according to the classical model; see Section 3.1 for details.)

However, this classical radiation model is not without issues. Perhaps the most conspicuous issue is the lack of energy conservation in the supersonic domain. Because the radiated wave carries power away from the surface vibration, the vibration should *lose* power as it propagates. The classical model, however, assumes the amplitude of the vibration to remain constant instead of decaying, thus neglecting any effects of this power loss on the vibration.

Furthermore, several articles over the last 30 years have reported results that are at odds with the classical model. Specifically, theoretical studies of leaky A_0 Lamb waves in solid plates immersed in fluids [9–14] and leaky Rayleigh waves on solid surfaces in contact with fluids [15] have found radiating waves even in the subsonic domain. According to the classical model, this subsonic radiation should not exist.

These articles are based on numerical solutions of exact equations for leaky Lamb and leaky Rayleigh waves. These equations account for the full and exact boundary conditions relating the component waves at the interface(s) between the solid and the fluid. This approach is well-established and well-founded in the physics of these types of waves, and is considered to be a standard and correct approach. However, expressing the problem through equations that are not only difficult to reason about, but which must also be solved numerically, makes this approach unsuited for gaining physical understanding of *why* subsonic radiation can occur. As several of these articles have commented on the remarkable presence of subsonic radiation [13–15] and none of them refer to a general explanation of the phenomenon, it is clear that the cause of subsonic radiation is not well understood.

Hence, the classical radiation model is evidently insufficient and should be superseded by a radiation model that can also describe the phenomenon of subsonic radiation from vibrating surfaces. A few related investigations have already been reported. Sandham et al. [16] showed subsonic radiation from a vibration with a time-varying amplitude that first increases exponentially before decreasing exponentially. However, their treatment is motivated by aeroacoustic problems that are not very relevant for the case of leaky surface vibrations. Furthermore, a general explanation of the subsonic radiation phenomenon is beyond the scope of their study.

To our knowledge, the only general physical explanation available in the literature is a brief qualitative justification by Mozhaev and Weihnacht [15] of why subsonic radiation is permissible. Their main insight is that because leaky vibrations are attenuated as their energy gradually radiates into the fluid, all radiated waves are *inhomogeneous* [17]. This means that the amplitude changes exponentially along each wavefront, as Fig. 2 shows.[1] (This is explained in more detail in Section 2, where we briefly cover the basic theory of inhomogeneous waves.) Because inhomogeneous waves propagate at a lower phase speed c than the speed c_f of homogeneous sound waves, inhomogeneous waves can propagate along the surface more slowly than homogeneous waves. Therefore, they argue, radiating waves can exist in part of the classical subsonic domain ($c_\mathrm{v} < c_\mathrm{f}$), so long as the vibrational phase speed c_v still exceeds the *inhomogeneous* wave phase speed c.

This justification by Mozhaev and Weihnacht has generality beyond their article's main topic of leaky Rayleigh waves. It implies that subsonic radiation can occur in some situations for *any* type of wave that can be modelled as an attenuated surface vibration

[1] An *evanescent* wave, as shown in Fig. 1c, is in our nomenclature an inhomogeneous wave propagating parallel to a surface, whose amplitude decays with the distance to the surface.

adjacent to a fluid. Fig. 2 shows three examples of such waves. However, while these authors' explanation is very credible, they do not flesh it out and test it thoroughly, and it has no predictive power on *which* situations allow subsonic radiation.

Hence, a better radiation model that can describe subsonic radiation is still required to fully understand the phenomenon. In turn, this improved understanding could allow design of, e.g., better techniques for measuring materials adjacent to vibrating surfaces as well as better microelectromechanical systems. A better model might also be used as an improved perturbation method to predict the attenuation of leaky surface vibrations. Multiple perturbation methods have already been derived for leaky Lamb waves using different approaches [18–20] but they all give the same numerical results [21,22], including an unphysical infinite discontinuity in the attenuation at coincidence.

In this article, we show how to build an enhanced radiation model that combines the central insight of Mozhaev and Weihnacht [15], namely that a radiating surface vibration must be attenuated, with the central insight of Watkins et al. [20], namely that the radiated power is balanced by a loss of power in the guided wave underlying the vibration. (We previously summarised preliminary results of this investigation in an extended abstract [23], and a related derivation has been done by Kiefer et al. [13].)

We build this radiation model under the assumption that the vibration is a *forward wave*, where the phase and the energy of the guided wave both propagate in the $+x$ direction. Plates also support a Lamb wave often called S_{2b}, which is a *backward wave* where phase and energy propagate in *opposite* directions of each other [24–27]. However, a full consideration of this phenomenon is outside the scope of our article.

In the rest of this article, we build and analyse the radiation model step by step and test it. Section 2 covers the necessary basics of inhomogeneous waves. In Section 3, we investigate the sound wave generated by a specified attenuated surface vibration, showing that *any* attenuated forward-wave vibration generates an outgoing wave. From the results of the investigation, we straightforwardly build the enhanced radiation model in Section 4, imposing conservation of energy by equating the power radiated by the inhomogeneous sound wave with the power lost in the surface vibration. Our hypothesis is that this model can correctly explain the mechanism underlying sound radiation from vibrating surfaces, including subsonic radiation. We test this hypothesis in the specific case of leaky A_0 Lamb waves in Section 5. Section 6 discusses what we have learned, and we conclude in Section 7.

2. Basic theory of inhomogeneous waves in lossless fluids

The rest of this article deals extensively with inhomogeneous plane waves in lossless fluids. This section summarises the basic theory of this lesser-known [17] type of wave. Advanced treatments on inhomogeneous waves in more complex media, such as viscoelastic solids, can be found in the literature [17,28,29].

We start with a straightforward generalisation of the plane sound wave in Eq. (2): we split the wavevector into a real and imaginary part as $\mathbf{k} = \mathbf{k}_\mathrm{r} + \mathrm{i}\mathbf{k}_\mathrm{i}$, so that $\mathrm{e}^{\mathrm{i}(\mathbf{k}\cdot\mathbf{r}-\omega t)} = \mathrm{e}^{\mathrm{i}(\mathbf{k}_\mathrm{r}\cdot\mathbf{r}-\omega t)}\,\mathrm{e}^{-\mathbf{k}_\mathrm{i}\cdot\mathbf{r}}$. The real part $\mathbf{k}_\mathrm{r}$ is a *propagation vector*, while the imaginary part $\mathbf{k}_\mathrm{i}$ is a *decay vector* that specifies the direction $\hat{\mathbf{k}}_\mathrm{i}$ and rate $|\mathbf{k}_\mathrm{i}| = k_\mathrm{i}$ of the decay. (Here and onward, the subscripts r and i indicate the real and imaginary part, respectively, and hats indicate unit vectors.) A wave where $k_\mathrm{i} = 0$ *or* $\mathbf{k}_\mathrm{i} \parallel \mathbf{k}_\mathrm{r}$ is called *homogeneous*, and a wave where $k_\mathrm{i} \neq 0$ *and* $\mathbf{k}_i \nparallel \mathbf{k}_r$ is called *inhomogeneous*.

After this split, the lossless wave dispersion relation in Eq. (3) immediately tells us that

$$\mathbf{k}\cdot\mathbf{k} = \mathbf{k}_\mathrm{r}\cdot\mathbf{k}_\mathrm{r} + 2\mathrm{i}\mathbf{k}_\mathrm{r}\cdot\mathbf{k}_\mathrm{i} - \mathbf{k}_\mathrm{i}\cdot\mathbf{k}_\mathrm{i} = k^2 = (\omega/c_\mathrm{f})^2, \tag{5}$$

which can only be true if $\mathbf{k}_\mathrm{r}\cdot\mathbf{k}_\mathrm{i} = 0$, which means that $\mathbf{k}_\mathrm{r}\perp\mathbf{k}_\mathrm{i}$. In other words, the directions of propagation and decay are perpendicular in a lossless medium. For simplicity, let us follow Poirée [29] and align a coordinate system $\mathbf{R} = (X, Y)$ with the wavefield, with the propagation vector $\mathbf{k}_\mathrm{r}$ in the X direction and the decay vector $\mathbf{k}_\mathrm{i}$ in the $\pm Y$ direction so that $\mathbf{k} = k_\mathrm{r}\hat{\mathbf{X}} \pm \mathrm{i}k_\mathrm{i}\hat{\mathbf{Y}}$. The plane wave in Eq. (2) then becomes

$$p(X, Y, t) = p_0\,\mathrm{e}^{\mathrm{i}(\mathbf{k}\cdot\mathbf{r}-\omega t)} = p_0\,\mathrm{e}^{\mathrm{i}(k_\mathrm{r}X-\omega t)}\,\mathrm{e}^{\mp k_\mathrm{i}Y}\,. \tag{6}$$

This shows that the amplitude stays constant along the direction of propagation, but decays or increases exponentially along the wavefronts. From Eqs. (5) and (6), we straightforwardly find that this wave has a phase speed

$$c = \frac{\omega}{k_\mathrm{r}} = \frac{\omega}{\sqrt{k^2 + k_\mathrm{i}^2}} = \frac{c_\mathrm{f}}{\sqrt{1 + \left(k_\mathrm{i}c_\mathrm{f}/\omega\right)^2}}, \tag{7}$$

which decreases from the speed of sound c_f as the inhomogeneity k_i increases.

The most basic example of an inhomogeneous wave is the evanescent wave in Fig. 1c. Fig. 2 sketches radiated inhomogeneous waves, where the wavefront amplitudes are constant along the characteristic lines in the propagation direction and the amplitude changes along the wavefronts. This amplitude change occurs because the amplitude of any point on a wavefront is proportional to the amplitude of the vibration at the point at the surface from which it was emitted. Therefore, as we follow a wavefront upward, we encounter wavefront segments of increasing amplitude because they were emitted increasingly far back on the surface, where the vibrational amplitude was higher.

For a theoretical *unbounded* forward-wave vibration of infinite extent, such as the classical model's vibration from Eq. (1), these amplitudes will gradually increase to infinity. In a more realistic *bounded* treatment where the vibration is instead excited at a specific location, the amplitude of the vibration and the radiated wavefronts will remain finite. Still, the radiated wavefield in the wedge-shaped radiation region starting at the excitation location is based on the unbounded solution [27]. The literature on guided wave propagation primarily considers theoretical unbounded waves, and dealing with bounded waves is beyond the scope of this article as well.

We can find the particle velocity $\mathbf{v}$ of the inhomogeneous wave by inserting its pressure, Eq. (6), into the linear Euler equation, which is valid for lossless fluids:

$$\rho\frac{\partial \mathbf{v}}{\partial t} = -\nabla p \qquad \Longrightarrow \qquad \mathbf{v}(X,Y,t) = \frac{\mathbf{k}}{\rho\omega}p(X,Y,t) = \frac{k_\mathrm{r}\hat{\mathbf{X}} \pm \mathrm{i}k_\mathrm{i}\hat{\mathbf{Y}}}{\rho\omega}p_0\,\mathrm{e}^{\mathrm{i}(k_\mathrm{r}X-\omega t)}\,\mathrm{e}^{\mp k_\mathrm{i}Y}. \tag{8}$$

Here, ρ is the fluid density. We see that while the particle motion of a homogeneous wave ($k_\mathrm{i} = 0$) is simply back and forth in the X direction with time, the particle motion of an inhomogeneous wave traces an ellipse in the X–Y plane.

3. Sound radiation from attenuated surface vibrations

The introduction showed that the classical radiation model, which imposes an *unattenuated* surface vibration, is unable to capture the phenomenon of subsonic radiation. However, we can generalise this surface vibration to represent *attenuated* surface vibrations by letting the surface wavenumber be *complex*:

$$k_x = k_{x\mathrm{r}} + \mathrm{i}k_{x\mathrm{i}} \qquad \Longrightarrow \qquad v_y(x, y=0, t) = v_{y0}\,\mathrm{e}^{\mathrm{i}(k_{x\mathrm{r}}x-\omega t)}\,\mathrm{e}^{-k_{x\mathrm{i}}x}. \tag{9}$$

As in Section 2, the real part $k_{x\mathrm{r}} > 0$ represents propagation with a phase speed $c_\mathrm{v} = \omega/k_{x\mathrm{r}}$ and the imaginary part $k_{x\mathrm{i}} \geq 0$ represents forward-wave attenuation.[2]

Even with a complex k_x, the rest of the derivation proceeds like before. However, expanding k_x into its real and imaginary parts in Eq. (4) shows that the wavevector y-component

$$k_y = \pm k\sqrt{\left[1 - \left(\frac{k_{x\mathrm{r}}}{k}\right)^2 + \left(\frac{k_{x\mathrm{i}}}{k}\right)^2\right] - \mathrm{i}\frac{2k_{x\mathrm{r}}k_{x\mathrm{i}}}{k^2}} = k_{y\mathrm{r}} + \mathrm{i}k_{y\mathrm{i}} \tag{10}$$

is always *complex* for a propagating wave ($k_{x\mathrm{r}} > 0$) whenever $k_{x\mathrm{i}} \neq 0$; it is no longer purely real or imaginary as in the classical model. We will take a closer look at the implications of this in Section 3.2.

3.1. Sound wavefields

Imposing an attenuated surface vibration generates a sound wave that can be expressed generally as:

$$p(x,y,t) = p_0\,\mathrm{e}^{\mathrm{i}(k_{x\mathrm{r}}x+k_{y\mathrm{r}}y-\omega t)}\,\mathrm{e}^{-k_{x\mathrm{i}}x}\,\mathrm{e}^{-k_{y\mathrm{i}}y}, \qquad \mathbf{v}(x,y,t) = \mathbf{v}_0\,\mathrm{e}^{\mathrm{i}(k_{x\mathrm{r}}x+k_{y\mathrm{r}}y-\omega t)}\,\mathrm{e}^{-k_{x\mathrm{i}}x}\,\mathrm{e}^{-k_{y\mathrm{i}}y}. \tag{11a}$$

The surface vibration in Eq. (9) acts as a boundary condition at $y = 0$ for the velocity $\mathbf{v}$, fixing its y-component amplitude to the vibrational amplitude v_{y0}. Furthermore, the pressure and velocity amplitudes p_0 and $\mathbf{v}_0$ are related as in Eq. (8), giving $\mathbf{v}_0 = (\mathbf{k}/\rho\omega)p_0$. From this, we can find explicit expressions for these amplitudes in terms of v_{y0} and $\mathbf{k}$:

$$\mathbf{v}_0 = \frac{\mathbf{k}v_{y0}}{k_y}, \qquad p_0 = \frac{\rho\omega v_{y0}}{k_y}. \tag{11b}$$

Fig. 3 shows the pressure fields from two attenuated surface vibrations, one supersonic and one subsonic. Both fields were plotted using the positive sign in Eq. (10) so that $k_{y\mathrm{r}} > 0$, which corresponds to an *outwards* propagating wave (as opposed to the negative sign giving an *inwards* propagating wave with $k_{y\mathrm{r}} < 0$). They both show waves propagating away from the surface at $y = 0$; while the subsonic wave radiates more parallel to the surface, it is not perfectly grazing like the evanescent wave in Fig. 1c.

In both cases, the waves are visibly inhomogeneous. The pressure increases exponentially as we follow a wavefront away from the surface, and the pressure goes to infinity with y. While this behaviour may seem troubling and has therefore led some to reject this solution [2], this behaviour is actually both *correct* and *necessary* for the field radiated from an unbounded attenuated surface vibration [13,15,30–32], as we explained in Section 2. Furthermore, for the attenuated forward-wave surface vibration in Eq. (9), this solution and the aforementioned inward propagating solution are the *only* valid wavefields in a lossless fluid.

A closer consideration of the real and imaginary wavevectors shown in Fig. 3 reveals why evanescent waves are not possible when the surface vibration is an attenuated forward wave ($k_{x\mathrm{i}} > 0$). Because the surface vibration and sound wavefield share k_x, the decay vector $\mathbf{k}_\mathrm{i}$ contains a strictly positive x component. We saw in Section 2 that $\mathbf{k}_\mathrm{r}$ and $\mathbf{k}_\mathrm{i}$ are always perpendicular in a lossless fluid, and because $\mathbf{k}_\mathrm{i}$ is not purely oriented along the y-axis, $\mathbf{k}_\mathrm{r}$ *cannot* be purely oriented along the x-axis (i.e, along the surface) as it would be for an evanescent wave. Instead, it will always point into the fluid.

We can also calculate the time-averaged intensity (i.e., power flow per area) from the pressure and velocity fields in Eq. (11) as

$$\mathbf{I}(x,y) = \mathrm{Re}\left\{\frac{\mathbf{v}(x,y,t)\overline{p}(x,y,t)}{2}\right\} = \mathbf{k}_\mathrm{r}\frac{\rho\omega|v_{y0}|^2}{2|k_y|^2}\,\mathrm{e}^{-2k_{x\mathrm{i}}x}\,\mathrm{e}^{-2k_{y\mathrm{i}}y}. \tag{12}$$

Here, the bar denotes complex conjugation, which can also be applied to the velocity instead of the pressure with the same result. We see that power flows in the direction of $\mathbf{k}_\mathrm{r}$. For all attenuated surface vibrations, we saw that $\mathbf{k}_\mathrm{r}$ will point into the fluid, and therefore, some power will be radiated away into the fluid as well. For evanescent waves, where $k_{y\mathrm{r}} = 0$, we find the well-known result [2] that they carry no power away from the surface.

[2] For a backward wave, energy would propagate in the $-x$ direction, opposite to the phase, so that attenuation due to radiation would entail $k_{x\mathrm{i}} < 0$ [27]. However, our further analysis will be limited to forward waves.

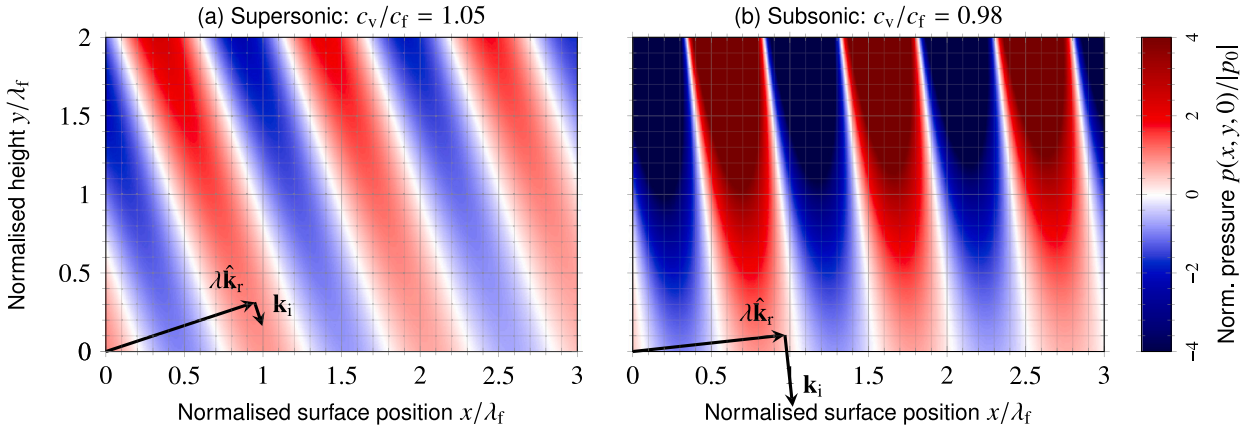

Fig. 3. Two pressure fields plotted as in Fig. 1, generated by *attenuated* vibrations ($k_{xi}/k = 0.025$) moving at two different phase speeds c_v.

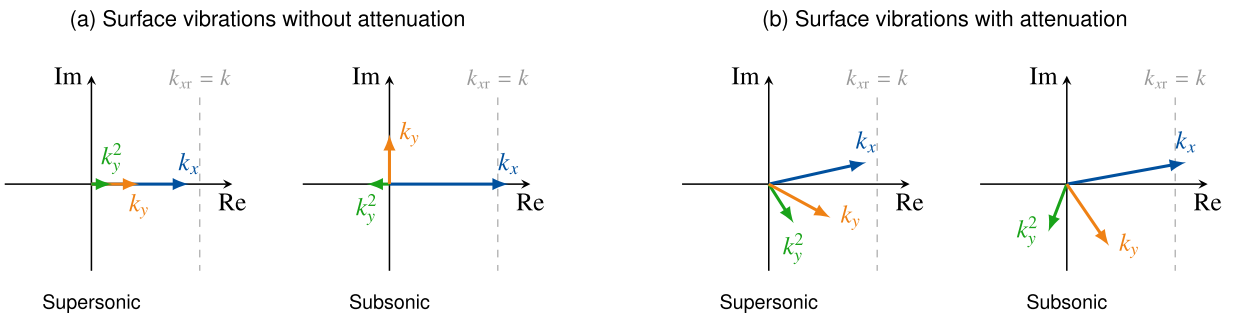

Fig. 4. Wavevector components k_x and k_y (via k_y^2) in the complex plane according to Eqs. (10) and (13), for supersonic and subsonic vibrations (a) without attenuation and (b) with attenuation. We use the positive root sign and for simplicity choose $k = 1$.

3.2. Interpretation of the wavevector y-component

Next, we investigate how the real and imaginary components of k_y behave around coincidence. While Eq. (10) can be decomposed into a series of explicit real and imaginary terms via Taylor expansion around $k_{xi}/k = 0$, the resulting Taylor series diverges near coincidence and is therefore of little use here. Instead, we can consider

$$k_y^2 = k^2 - (k_{xr} + \mathrm{i}k_{xi})^2 = \left(k^2 - k_{xr}^2 + k_{xi}^2\right) - \mathrm{i}2k_{xr}k_{xi}, \tag{13}$$

which is already decomposed in a real and an imaginary part. Plotting k_x and the resulting k_y^2 on the complex plane, as in Fig. 4, lets us conveniently reason about the behaviour of $k_y = \sqrt{k_y^2}$. When doing so, we will only consider surface vibrations that propagate as forward waves in the x direction ($k_{xr} > 0$). These may either have zero attenuation ($k_{xi} = 0$, Fig. 4a) or nonzero attenuation in the x direction ($k_{xi} > 0$, Fig. 4b). We discount solutions corresponding to incoming waves ($k_{yr} < 0$).

First, let us consider the unattenuated surface vibrations in Fig. 4a. In the supersonic case ($k_x < k$), k_y^2 is real and positive, leading to a real and positive k_y, i.e., outward radiation. In the subsonic case ($k_x > k$), however, k_y^2 is real and *negative*, leading to a *positive imaginary* k_y — an evanescent wave, as shown in Fig. 1c.[3]

Next, let us consider the attenuated surface vibrations in Fig. 4b. In both the supersonic and the subsonic cases, k_y^2 can be found in the 3rd or 4th quadrants of the complex plane, with a negative imaginary part. Therefore, k_y can always be found in the 4th quadrant, with $k_{yr} > 0$ and $k_{yi} < 0$.

In other words, *every* attenuated surface vibration propagating as a forward wave in the x direction ($k_{xr} > 0$, $k_{xi} > 0$) radiates a wave away into the fluid ($k_{yr} > 0$) whose pressure increases exponentially with the distance to the surface ($k_{yi} < 0$). This corroborates our discussion in Section 3.1.

[3] We made a deliberate choice to use the $e^{i(\mathbf{k}\cdot\mathbf{r}-\omega t)} = e^{i(\mathbf{k}_r\cdot\mathbf{r}-\omega t)}e^{-\mathbf{k}_i\cdot\mathbf{r}}$ convention in this article instead of the $e^{i(\omega t-\mathbf{k}\cdot\mathbf{r})} = e^{i(\omega t-\mathbf{k}_r\cdot\mathbf{r})}e^{\mathbf{k}_i\cdot\mathbf{r}}$ convention. With the former convention, the principal root $k_y = \sqrt{k_y^2}$ is always the desired solution. With the latter convention, $\mathbf{k}_i$ represents exponential *increase* instead of *decay*, and therefore we would need to choose the other root in the case of evanescent waves where the principal root $\sqrt{k_y^2}$ is positive.

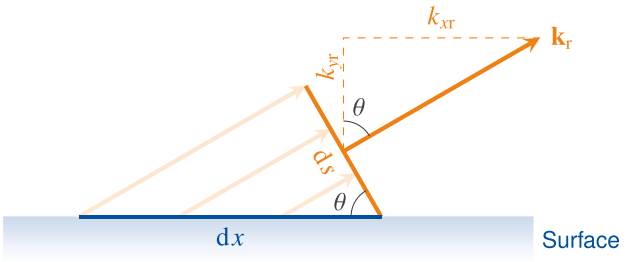

Fig. 5. An infinitesimal wavefront segment ds and its surface projection dx for a plane wave with propagation wavevector $\mathbf{k}_r$ and radiation angle θ.

3.3. Properties of the radiated sound wave

With the sound wavevector components k_x and k_y known, we can calculate various properties of the sound wave over a range of vibrational phase speeds c_v, for example, radiated intensity, radiation angle, and the phase speed of the emitted wave.

We begin with considering the time-averaged intensity vector $\mathbf{I}$ in Eq. (12). In *two* spatial dimensions, its magnitude represents the power per unit *length* perpendicular to its orientation; in this case, along the wavefronts. However, to relate the radiated power to power lost in the surface vibration, we need to know the power radiated into the fluid per unit length *along the surface*, which we represent as I_{rad}. From Fig. 5, we see that all of the power along the infinitesimal wavefront segment ds has been radiated from its surface projection dx. In other words, $I_{\text{rad}}\mathrm{d}x = I\mathrm{d}s$, and hence

$$I_{\text{rad}}(x) = I(x,0)\frac{\mathrm{d}s}{\mathrm{d}x} = I(x,0)\cos\theta = I_y(x,0) = \frac{k_{yr}}{|k_y|^2}\frac{\rho\omega|v_{y0}|^2}{2}\mathrm{e}^{-2k_{xi}x} = \frac{k_{yr}/k}{|k_y/k|^2}\frac{\rho c_f|v_{y0}|^2}{2}\mathrm{e}^{-2k_{xi}x}. \tag{14a}$$

Note that the radiated intensity I_{rad} equals the intensity y-component I_y at the surface. Next, the radiated sound wave's radiation angle θ can be found from Fig. 5 to be

$$\theta = \arctan\left(\frac{k_{xr}}{k_{yr}}\right) = \arctan\left(\frac{k_{xr}/k}{k_{yr}/k}\right). \tag{14b}$$

Finally, its phase speed can be found from Eq. (11) to be

$$c = \frac{\omega}{|\mathbf{k}_r|} = \frac{kc_f}{\sqrt{k_{xr}^2 + k_{yr}^2}} = \frac{c_f}{\sqrt{\left(k_{xr}/k\right)^2 + \left(k_{yr}/k\right)^2}}. \tag{14c}$$

The three properties of radiated intensity amplitude $I_{\text{rad},0}$, radiation angle θ, and wave phase speed c can all be expressed in normalised form so that they only depend on the normalised surface wavenumber's real part k_{xr}/k and imaginary part k_{xi}/k (in some cases via k_y/k — see Eq. (10)):

$$\frac{I_{\text{rad},0}}{\rho c_f|v_{y0}|^2/2} = \frac{k_{yr}/k}{|k_y/k|^2}, \qquad \theta = \arctan\left(\frac{k_{xr}/k}{k_{yr}/k}\right), \qquad \frac{c}{c_f} = \left[\left(k_{xr}/k\right)^2 + \left(k_{yr}/k\right)^2\right]^{-1/2}. \tag{15}$$

Fig. 6 plots each of these normalised properties against the normalised vibrational phase speed $c_v/c_f = k/k_{xr}$ for different choices of normalised attenuation k_{xi}/k.

First, we consider the behaviour of all three properties for an unattenuated surface vibration ($k_{xi} = 0$). We look from the supersonic domain, past coincidence, and into the subsonic domain, i.e., right-to-left in each subplot of Fig. 6. The radiated intensity in Fig. 6a increases towards an infinite discontinuity at coincidence, with zero radiated intensity in the subsonic domain. The radiation angle in Fig. 6b increases towards coincidence where it reaches a 90° grazing angle that persists in the subsonic domain, as it becomes an evanescent wave as shown in Fig. 1c. The phase speed in Fig. 6c changes sharply from c_f in the supersonic domain to c_v in the subsonic domain.

With attenuation, we see a smoothing effect around coincidence. As the attenuation increases, the sharp changes that occur at coincidence for an unattenuated vibration become increasingly smooth. Far into the subsonic and the supersonic domain, the properties go *asymptotically* towards the unattenuated properties. For the radiated intensity (Fig. 6a), the discontinuity disappears, and there is a nonzero radiation of power in the entire subsonic domain. The radiation angle (Fig. 6b) never quite reaches a grazing angle in the subsonic domain. As for the phase speed of the subsonically radiating waves (Fig. 6c), we can see that $c < c_v$, like Mozhaev and Weihnacht concluded [15].

Finally, note that as long as the vibration is an attenuated forward wave ($k_{xi} > 0$), then no matter how far we go into the subsonic domain or how small the vibrational attenuation k_{xi} is, we still find a negative k_{yi}, corresponding to an exponential *increase* with y of the sound wavefields. Only when the vibration is perfectly unattenuated ($k_{xi} = 0$) can we find a positive k_{yi}, corresponding to an exponential decrease with y. In fact, the conventionally rejected solution $k_y = -\mathrm{i}k\sqrt{(c_f/c_v) - 1}$ of the classical model, which we briefly discussed in Section 1, may be viewed as the limit $\lim_{k_{xi}\to 0} k_y$ of the outgoing attenuated solution in the subsonic domain.

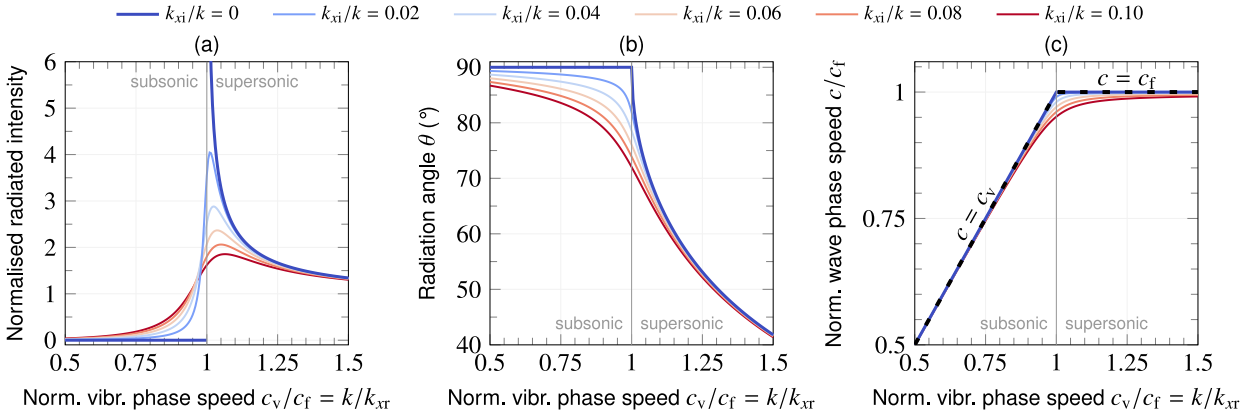

Fig. 6. Properties of the inhomogeneous wave radiated from a surface vibration for several fixed values of the attenuation k_{xi}. All properties are normalised as in Eq. (15). (a) Normalised radiated intensity amplitude. (b) Radiation angle. (c) Normalised phase speed, with black dashed lines indicating where $c = c_v$ and $c = c_f$.

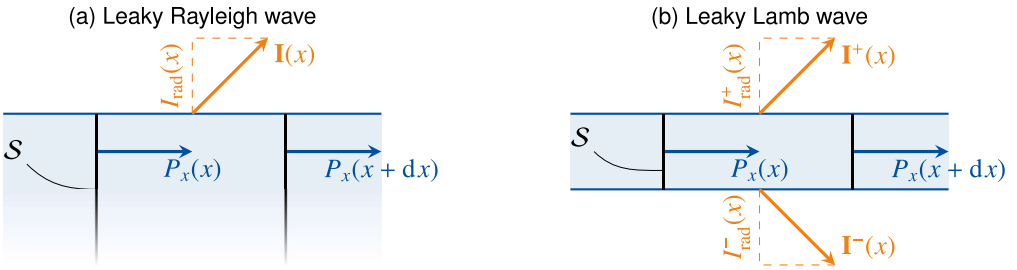

Fig. 7. Power balance for two types of guided waves. The loss in power flow P_x in the interval $[x, x + dx]$ must equal the total power radiation into the fluid inside the same interval. (a) Leaky Rayleigh wave, with power radiation on one side and a semi-infinite cross-section $\mathcal{S}$. (b) Leaky Lamb waves, with power radiation on both sides and a finite cross-section $\mathcal{S}$. With the same fluid on both sides of the plate and vibrational similarity between the Rayleigh and Lamb waves, then $|\mathbf{I}^+| = |\mathbf{I}^-| = |\mathbf{I}|$ and $I^+_{rad} = I^-_{rad} = I_{rad}$.

4. An energy-conserving radiation model

In Section 3, we simply imposed an arbitrary surface vibration and analysed the resulting sound wave in the fluid. However, surface vibrations are typically caused by some kind of guided wave, such as a Lamb or Rayleigh wave (Figs. 2 and 7), which carries a certain amount of power. For a physically valid treatment, we must take conservation of energy into account, balancing the power that the sound wave radiates away into the fluid with a loss of power in the guided wave. However, finding this balance is complicated by the fact that the loss of power in the guided wave determines the attenuation of the surface vibration, which in turn strongly affects the radiated intensity close to and below coincidence, as we saw in Section 3.3 and Fig. 6a.

First, to be able to express the effect of this power loss, we must first quantify the power contained in the guided wave. It can be expressed as the power flow [13,19,20,27], which is the integral of the time-averaged intensity inside the solid over its cross-section $\mathcal{S}$ shown in Fig. 7:

$$P_x(x) = \int_{\mathcal{S}} \mathbf{I}(x, y) \cdot \mathrm{d}\boldsymbol{\mathcal{S}} = \int_{\mathcal{S}} I_x(x, y)\mathrm{d}y = P_{x0}\, \mathrm{e}^{-2k_{xi}x}. \tag{16}$$

$\mathbf{I}$ gets its x dependence $\mathrm{e}^{-2k_{xi}x}$ from being the product of two wavefield components propagating as $\mathrm{e}^{\mathrm{i}(k_{xr}x-\omega t)}\,\mathrm{e}^{-k_{xi}x}$, with one component complex conjugated as in Eq. (12). We will come back to calculating I_{x0} and P_{x0} for the specific case of a Lamb wave in Section 5.

4.1. The enhanced radiation model equation

If there are no other sources of power loss in the guided wave, the radiated power per unit length must equal the power loss per unit length. For one-sided radiation, as illustrated in Fig. 7a, this power balance is expressed as

$$I_{rad}(x) = -\frac{\mathrm{d}P_x}{\mathrm{d}x}(x) = 2k_{xi}P_x(x). \tag{17}$$

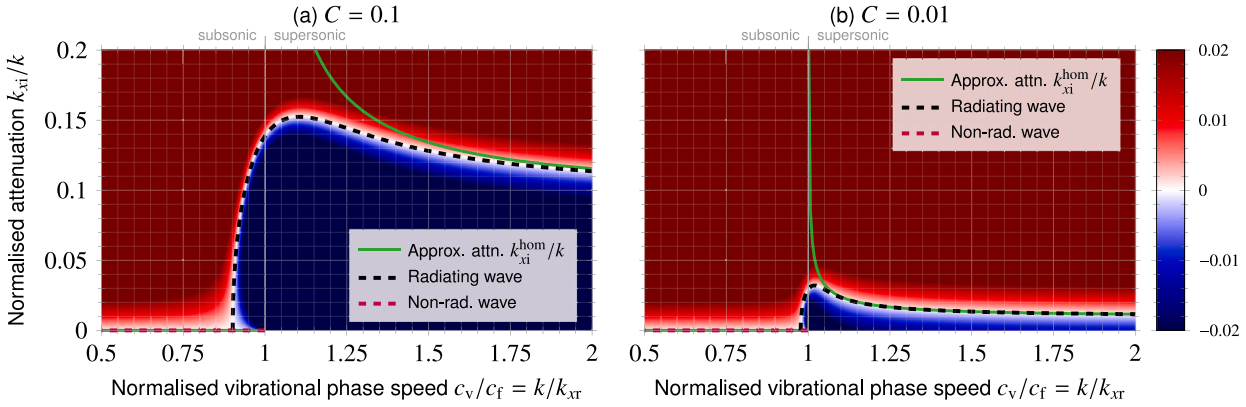

Fig. 8. Surface plots of g from Eq. (20). Its roots, which represent propagating waves, are shown as dashed lines. The approximate attenuation from Eq. (19) is shown as a solid line. (a) More strongly radiating wave ($C = 0.1$). (b) Less strongly radiating wave ($C = 0.01$).

(For two-sided radiation into the same fluid as in Fig. 7b, we simply replace I_{rad} with $2I_{rad}$ here and later.) From Eqs. (10) and (14a), we know that the intensity amplitude $I_{rad,0}$ is a function of k_{xr} and k_{xi} via k_y. Similarly, the power flow amplitude P_{x0} may have an k_{xr} and k_{xi} dependence as well. Hence, we can express Eq. (17) as an implicit equation defining a radiation model

$$f(k_{xr}, k_{xi}) = k_{xi} - \frac{I_{rad,0}(k_{xr}, k_{xi})}{2P_{x0}(k_{xr}, k_{xi})} = k_{xi} - \frac{k_{yr}}{|k_y|^2}\frac{\rho\omega|v_{y0}|^2}{4P_{x0}} = 0, \tag{18}$$

where we have used Eq. (14a) for the last equality. Its roots $f(k_{xr}, k_{xi}) = 0$ represent combinations of k_{xr} and k_{xi} that respect conservation of energy, so that the loss in power flow matches the radiated intensity. This implicit equation can also be seen as defining an implicit function for k_{xi}, which for a given k_{xr} may be solved by an iterative root-finding algorithm.

Explicit versions of Eq. (18) have previously appeared in the literature, for example in [20] by Watkins et al. who pioneered the above power balance approach but did not take the inhomogeneity of the radiated wave into account. We may similarly make Eq. (18) explicit through approximation: specifically, we assume v_{y0} and P_{x0} to be constant and approximate the radiated waves as being homogeneous by substituting k_y with $k_y^{hom} = k\sqrt{1-(k_{xr}/k)^2}$. Because $k_y^{hom} = k_{yr}^{hom} = |k_y^{hom}| = k\cos(\theta^{hom})$ in the supersonic domain (with $\theta^{hom} = \arctan(k_{xr}/k_{yr}^{hom})$) and $k_{yr}^{hom} = 0$ in the subsonic domain, these substitutions let us directly solve Eq. (18) to find

$$k_{xi} \approx k_{xi}^{hom} = \begin{cases} \frac{\rho c_f |v_{y0}|^2}{4P_{x0}\cos(\theta^{hom})} & \text{for } k_{xr}/k < 1 \text{ (supersonic domain)}, \\ \text{undefined} & \text{for } k_{xr}/k = 1 \text{ (coincidence)}, \\ 0 & \text{for } k_{xr}/k > 1 \text{ (subsonic domain)}. \end{cases} \tag{19}$$

k_{xi}^{hom} is the approximate attenuation derived by Auld [12,19] through a more involved perturbation approach based on the complex reciprocity relation. In other words, we can reproduce Auld's result as an approximation of Eq. (18), which is not only more straightforward to derive than Auld's result, but also more general as it can take the inhomogeneity of the radiated sound wave into account.

Furthermore, Kiefer et al. [13] also followed the same power balance approach to derive an equation $\alpha = I_{y0}(h)/2P_{x0}$ which is very similar to part of Eq. (18). Here, α is the attenuation due to radiation and h is the y coordinate of the top surface. They calculate $I_{y0}(h)$ and P_{x0} numerically from a provided exact leaky Lamb wavefield in a plate with a fluid on only one side. Using this provided wavefield, their equation can be calculated explicitly and $I_{y0}(h)$ includes inhomogeneity thanks to the inherent attenuation k_{xi} of the wavefield. While their $I_{y0}(h)$ derives from the wavefield inside the solid, our $I_{rad,0}$ derives from the wavefield of the inhomogeneous fluid wave. Although both wavefields' intensities $I_{y0}(h)$ and $I_{rad,0}$ are evaluated at the fluid–solid interface where their y-components are equal, our choice allows using the simple analytical form of Eq. (14a), making Eq. (18) more amenable to further analysis.

While finding the roots of Eq. (18) analytically is not feasible, except in some limits that we will discuss in Section 4.2, these roots are not difficult to find numerically. For generality, we will investigate the roots of a normalised version of the radiation model equation:

$$g\left(k_{xr}/k, k_{xi}/k\right) = \frac{k_{xi}}{k} - \frac{k_{yr}/k}{|k_y/k|^2}C = 0, \qquad \text{with} \qquad C = \frac{\rho c_f |v_{y0}|^2}{4kP_{x0}}. \tag{20}$$

The dimensionless *radiation factor* C expresses a ratio between the radiation efficiency of the sound wave and the power of the guided wave. It can also be related to the approximate attenuation k_{xi}^{hom} in the supersonic domain as $C = k_{xi}^{hom}\cos(\theta^{hom})/k$. In other words, higher C values imply higher attenuations.

Fig. 8 shows surface plots of $g(k_{xr}/k, k_{xi}/k)$ for two different radiation factors C, with the roots indicated as dashed lines. In both cases, we find two branches of roots, representing two propagating waves. One is an unattenuated wave ($k_{xi} = 0$) that exists only in the subsonic domain, which corresponds to the classical evanescent subsonic solution covered in Section 1 and shown in Fig. 1c. This wave trivially satisfies energy conservation as no power is radiated into the fluid or lost in the guided wave. However, the other wave is radiating ($k_{xi} > 0$) and exists in the entire supersonic domain and part of the subsonic domain. Hence, there is a subsonic subdomain where both waves are valid solutions of the radiation model in Eq. (18).

The classical approximate attenuation k_{xi}^{hom} is also plotted in Fig. 8 for comparison. It reaches an infinite discontinuity at coincidence and is zero in the subsonic domain. The attenuation curve of our radiating wave, on the other hand, qualitatively matches exact solutions for subsonic leaky A_0 Lamb waves in the literature [10,12–14,33]. Furthermore, comparing Figs. 8a and b, we can see that the more strongly radiating vibration stretches further into the subsonic domain before it is cut off. This qualitatively matches what Dabirikhah and Turner found for a leaky A_0 Lamb wave as they artificially increased the density of the fluid surrounding the solid plate [10].

These similarities lead us to a hypothesis that the enhanced radiation model is a correct description of the mechanism underlying sound radiation from vibrating surfaces. From this hypothesis, we can make a testable prediction that if we find exact values for the wavenumber k_x, the radiated intensity $I_{\text{rad},0}$, and the power flow P_{x0} for a subsonic leaky guided wave, inputting these values into the radiation model in Eq. (18) will show that the exact guided wave solution is a root of this equation. While a sufficiently equivalent test for the first equality of Eq. (18) has already been performed by Kiefer et al. [13] for the case of a brass plate in contact with water on one side, we test this prediction for other leaky Lamb wave cases exhibiting a wider variety of behaviours in Section 5.

The approximate attenuation k_{xi}^{hom} assumes the radiated wave to be homogeneous, while the radiating waves shown in Fig. 8 do not. The differences between the two underline the importance of taking the inhomogeneity of radiated waves into account close to coincidence. Because the inhomogeneity is a direct result of the attenuation of the surface vibration, we also see that k_{xi}^{hom} is a worse approximation for the more attenuated wave in Fig. 8a than for the less attenuated wave in Fig. 8b, even far into the supersonic domain.

4.2. Characteristics of the radiating wave

The normalised radiation model in Eq. (20) can be seen as an implicit function $\frac{k_{xi}}{k}(\frac{c_v}{c_f}, C)$ for the normalised attenuation. While deriving an explicit function for this attenuation may not be possible, we can still determine some characteristics of the radiating wave's attenuation curve. This section summarises the results from the full discussion in the Appendix.

As Fig. 8 indicates, more strongly radiating waves extend further into the subsonic domain before they are cut off. The normalised vibrational phase speed $c_{v,\text{cutoff}}/c_f$ at which this cutoff occurs is given by

$$\frac{\left[(c_f/c_{v,\text{cutoff}})^2 - 1\right]^{3/2}}{c_f/c_{v,\text{cutoff}}} = C, \qquad \frac{c_{v,\text{cutoff}}}{c_f} \approx \frac{1}{1 + C^{2/3}/2}. \tag{21}$$

Here, the first equation is an exact implicit function and the second is an approximate explicit function. Fig. 9a compares these two cutoff speeds. The explicit approximation is remarkably accurate despite being based on a lowest-order series expansion of the exact implicit function, with a maximum absolute error of 0.015. The figure also demonstrates a subsonic radiation cutoff behaviour that we could only guess at from Fig. 8: in the limit of weak radiation ($C \to 0$), the cutoff speed goes asymptotically to the classical coincidence result $c_{v,\text{cutoff}} = c_f$, while in the limit of strong radiation ($C \to \infty$), the cutoff speed goes asymptotically to 0.

While earlier perturbation methods to find the attenuation of the radiating wave [18–20] predict an infinite discontinuity in the attenuation at coincidence ($c_v = c_f$), Fig. 8 shows that the enhanced radiation model instead predicts a finite attenuation. In the limits of low and high C, this attenuation at coincidence is

$$\frac{k_{xi}}{k}(c_v = c_f) \approx \begin{cases} (C/2)^{2/3} & \text{for } C \ll 1, \\ \sqrt{C} & \text{for } C \gg 1. \end{cases} \tag{22}$$

Fig. 9b compares these approximations of coincidence attenuation with values determined numerically from Eq. (20).

Fig. 8 shows that the attenuation curve peaks close to coincidence, with a value $k_{xi,\text{peak}}/k$ at the relative phase speed $c_{v,\text{peak}}/c_f$. For larger C, Fig. 8 indicates that these peaks are taller and further away from coincidence. The peaks also become less prominent; in fact, numerical investigation shows that these attenuation peaks no longer occur above $C \approx 0.866$. Above this value of C, the attenuation simply increases monotonically with c_v. For lower values of C, however, the peaks can be approximately characterised by

$$\frac{k_{xi,\text{peak}}}{k} \approx \frac{1}{a + bC^{-2/3}}, \qquad \frac{c_{v,\text{peak}}}{c_f} \approx 1 + \frac{1}{c + dC^{-2/3}}, \tag{23a}$$

where

$$a = -0.19195482, \qquad b = 1.4547858, \qquad c = -2.0919058, \qquad d = 2.5193662. \tag{23b}$$

Fig. 9c compares these approximations with values determined numerically from Eq. (20). The $k_{xi,\text{peak}}/k$ fit is very good over the entire range of validity, while the $c_{v,\text{peak}}/c_f$ fit is only good up to $C \approx 0.2$ as the peak starts moving very rapidly into the supersonic domain as C approaches 0.866.

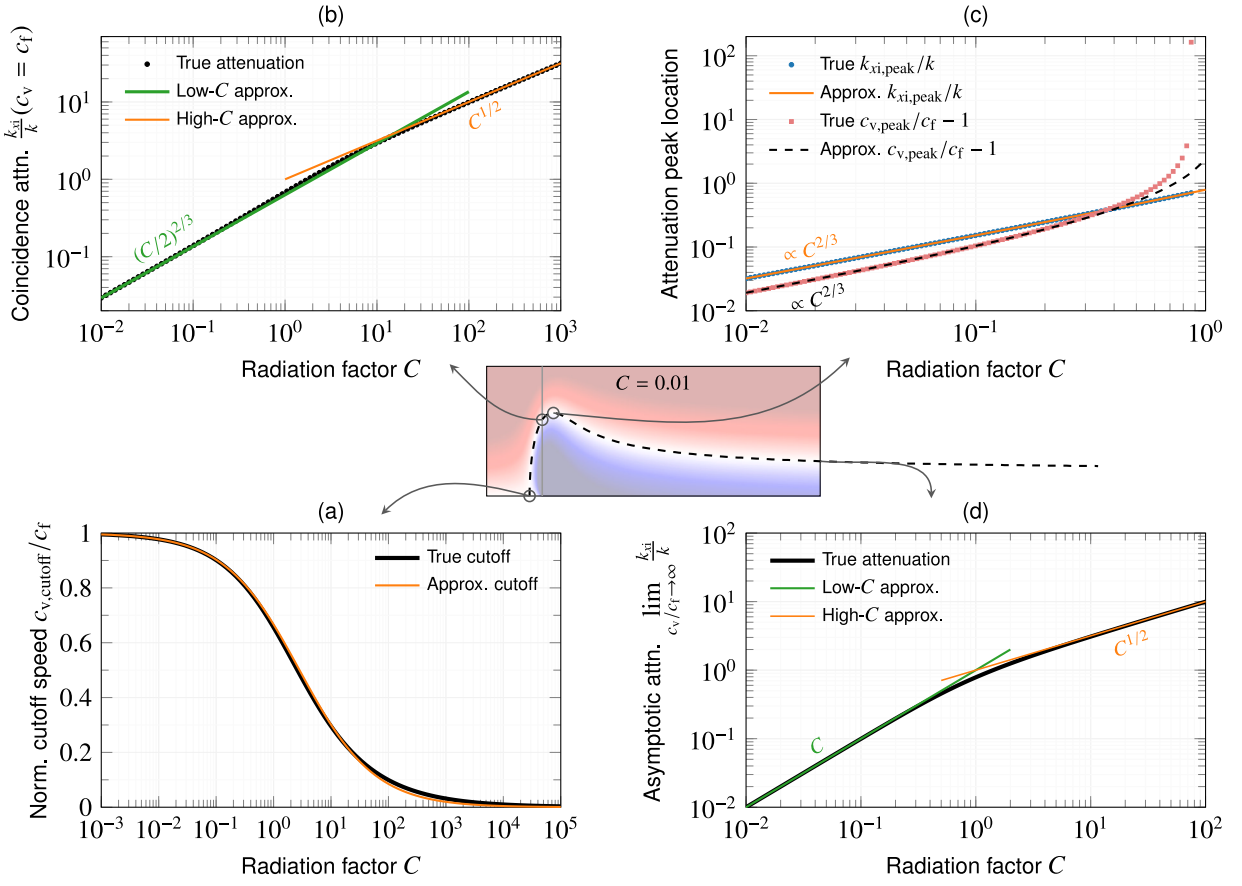

Fig. 9. Various characteristics of the radiating wave, as indicated on the central figure corresponding to Fig. 8b, against the radiation factor C. Lines represent analytical expressions, while dots represent values sampled numerically from the normalised model equation Eq. (20).

Fig. 8 also indicates that the attenuation goes asymptotically towards a particular value in the supersonic domain. This value can be derived to be

$$\lim_{(c_v/c_f)\to\infty} \frac{k_{xi}}{k} = \sqrt{\frac{\sqrt{1+4C^2}-1}{2}} \approx \begin{cases} C & \text{for } C \ll 1, \\ \sqrt{C} & \text{for } C \gg 1, \end{cases} \tag{24}$$

and is plotted against its low- and high-C approximations in Fig. 9d.

The above approximations let us more easily reason about how the attenuation curve evolves with C. For low values of C, the peak attenuation increases with $C^{2/3}$ while the asymptotic supersonic attenuation is approximately C. Hence, at some point the asymptotic supersonic attenuation catches up with the peak attenuation, so that the peak disappears, as mentioned above. For high values of C, the attenuation at coincidence and in the supersonic limit both go to $\sqrt{C}$, so that the attenuation curve reaches its asymptotic supersonic value already at coincidence.

5. Testing against leaky A_0 Lamb waves

We now test the energy-conserving radiation model in Eq. (18) against numerical solutions of the exact equations for leaky A_0 Lamb waves in a plate immersed in a fluid. A_0 is the lowest-order antisymmetric Lamb mode. (Fig. 10 shows the phase speeds of various Lamb modes in *free* – meaning vacuum-immersed – plates. These free-plate phase speeds are largely very similar to those of plates immersed in light fluids [13,18,33].) At low frequencies, A_0 waves are approximately flexural waves with a phase speed $c_v \propto \sqrt{fd}$, d being the plate thickness. At very high frequencies, the A_0 (as well as S_0) waves are akin to Rayleigh waves propagating on each side of the plate at a phase speed c_v that goes asymptotically with fd to the Rayleigh wave speed c_R, which is only slightly lower than the plate material's S-wave speed c_S [19]. Therefore, with reference to Fig. 10, as long as the fluid's speed of sound is smaller than the Rayleigh wave speed ($c_f < c_R$), the A_0 wave will *always* experience a subsonic-to-supersonic transition at a certain *coincidence frequency* f_c. Because the A_0 wave's phase speed c_v increases monotonically with f, $f < f_c$ corresponds to the subsonic domain and $f_c < f$ corresponds to the supersonic domain.

We perform two tests of the enhanced radiation model against the behaviour around this transition:

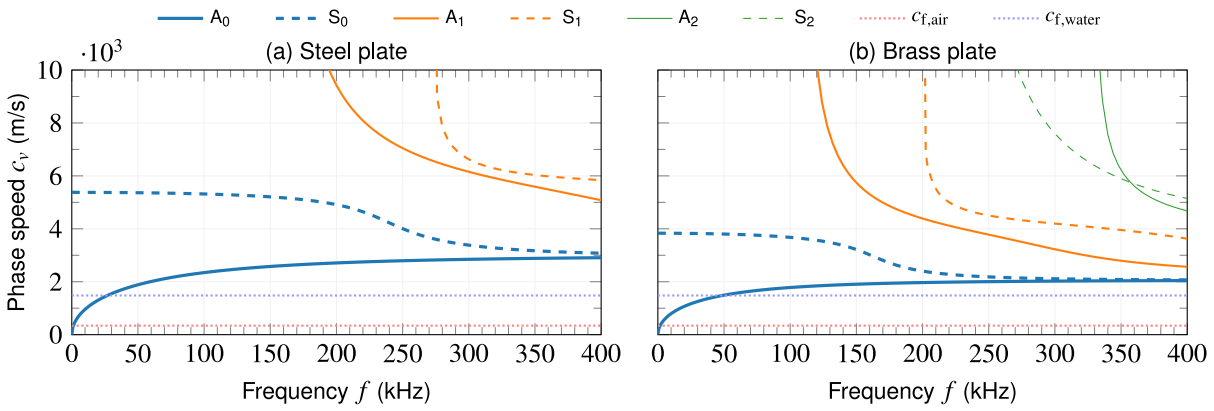

Fig. 10. Phase speeds of Lamb modes in free plates of thickness $d = 1$ cm made of (a) steel and (b) brass, with material parameters as in Table 1. Antisymmetric and symmetric modes of order n are indicated as A_n and S_n, respectively. These curves were found via the mode tracing method of [22].

1. We investigate whether this model can be used as a perturbation method for estimating the attenuation of *leaky* A_0 waves from the dispersion and wavefields of *free* A_0 Lamb waves in a plate in a vacuum. This approach assumes that the fluid immersion can be treated as a small perturbation to the free-plate situation, similarly to existing perturbation methods in the literature [18–20]. Despite differing approaches, these previous methods all give numerically identical results [21,22]. These results correspond to $k_{\mathrm{xi}}^{\mathrm{hom}}$ in Eq. (19), which assumes homogeneous sound radiation corresponding to the classical model, leading to weaknesses around coincidence shown in Fig. 8 and discussed in Section 4.1.
2. We validate the correctness of the radiation model equation by quantitatively checking it against solutions of the exact leaky Lamb wave equations.

When applying Eq. (18) to leaky A_0 Lamb waves, we must take into account that the plate radiates a wave from its surfaces on *both* sides, with a total radiated intensity *twice* the single-sided radiated intensity of Eq. (14a) as explained in Section 4.1.

5.1. Dispersion and wavefields of A_0 Lamb waves

Characterising the surface vibration in the radiation model in Eq. (18) requires some properties of the A_0 Lamb wave. For each angular frequency ω of interest, we need the real part of the surface wavenumber k_{xr}, the velocity magnitude $|v_{y0}|$ at the plate surface, and the power flow amplitude P_{x0}.

For free antisymmetric Lamb modes, the real-valued wavenumber k_x can be obtained at a given frequency by solving a transcendental dispersion relation for antisymmetric Lamb modes [1,22,34,35],

$$\frac{\tan(\gamma_{\mathrm{P}} h)}{\tan(\gamma_{\mathrm{S}} h)} + \frac{4k_x^2 \gamma_{\mathrm{S}} \gamma_{\mathrm{P}}}{(k_x^2 - \gamma_{\mathrm{S}}^2)^2} = 0. \tag{25}$$

Here, $h = d/2$ is half of the plate thickness d; with the plate centred on the x–z plane, its boundaries lie at $y = \pm h$. Solids support both longitudinal P-waves with a speed c_{P} and transversal S-waves with a speed c_{S}, and the variables γ_{P} and γ_{S} represent the y-components of the P- and S-wavevectors inside the plate, respectively:

$$\gamma_{\mathrm{P}}^2 = \frac{\omega^2}{c_{\mathrm{P}}^2} - k_x^2. \qquad \gamma_{\mathrm{S}}^2 = \frac{\omega^2}{c_{\mathrm{S}}^2} - k_x^2. \tag{26}$$

Solving Eq. (25) for the A_0 dispersion curve is not immediately straightforward because of its implicit nature, and solutions must be found numerically. Furthermore, additional anti-symmetric modes (A_1, A_2, etc.) are introduced at their corresponding cut-off frequencies. Here we take the solutions for granted, but methods for obtaining and tracing the dispersion curves are discussed thoroughly in, e.g., [22,34,36].

Once the dispersion relation for the A_0 mode is known, the remaining properties can be obtained from the Lamb wavefields associated with antisymmetric modes, which can be found by combining the wavefields of the component P- and S-waves that the Lamb waves comprise. The resulting velocity and stress components can be expressed as [22,37,38]:

$$v_x^{\mathrm{A}}(x,y,t) = \mathrm{i}\omega K \left[k_x \sin(\gamma_{\mathrm{P}} y) - \gamma_{\mathrm{S}} R^{\mathrm{A}} \sin(\gamma_{\mathrm{S}} y)\right] \mathrm{e}^{\mathrm{i}(k_x x - \omega t)}, \tag{27a}$$

$$v_y^{\mathrm{A}}(x,y,t) = \omega K \left[\gamma_{\mathrm{P}} \cos(\gamma_{\mathrm{P}} y) + k_x R^{\mathrm{A}} \cos(\gamma_{\mathrm{S}} y)\right] \mathrm{e}^{\mathrm{i}(k_x x - \omega t)}, \tag{27b}$$

$$\sigma_{xx}^{\mathrm{A}}(x,y,t) = \mathrm{i}KG \left[(2\gamma_{\mathrm{P}}^2 - k_x^2 - \gamma_{\mathrm{S}}^2) \sin(\gamma_{\mathrm{P}} y) + 2k_x \gamma_{\mathrm{S}} R^{\mathrm{A}} \sin(\gamma_{\mathrm{S}} y)\right] \mathrm{e}^{\mathrm{i}(k_x x - \omega t)}, \tag{27c}$$

$$\sigma_{xy}^{\mathrm{A}}(x,y,t) = -KG \left[2k_x \gamma_{\mathrm{P}} \cos(\gamma_{\mathrm{P}} y) + (k_x^2 - \gamma_{\mathrm{S}}^2) R^{\mathrm{A}} \cos(\gamma_{\mathrm{S}} y)\right] \mathrm{e}^{\mathrm{i}(k_x x - \omega t)}, \tag{27d}$$

$$\sigma_{yy}^{\mathrm{A}}(x,y,t) = \mathrm{i}KG \left[(k_x^2 - \gamma_{\mathrm{S}}^2) \sin(\gamma_{\mathrm{P}} y) - 2k_x \gamma_{\mathrm{S}} R^{\mathrm{A}} \sin(\gamma_{\mathrm{S}} y)\right] \mathrm{e}^{\mathrm{i}(k_x x - \omega t)}, \tag{27e}$$

Table 1
Material parameters.

Material	ρ (kg/m^3)	c_P (m/s)	c_S (m/s)
Air	1.21	340	–
Water	1000	1480	–
Steel	7850	5900	3200
Brass	8440	4480	2200

where

$$R^\mathrm{A} = \frac{(k_x^2 - \gamma_\mathrm{S}^2)\sin(\gamma_\mathrm{P} h)}{2k_x\gamma_\mathrm{S}\sin(\gamma_\mathrm{S} h)} \tag{27f}$$

is the amplitude ratio between the component S- and P-waves [22] for a free antisymmetric Lamb wave, G is the shear modulus, and K is an arbitrary scaling amplitude. The velocity magnitude $|v_{y0}|$ at the plate surface can be found by evaluating Eq. (27b) at $y = \pm h$. The power flow amplitude P_{x0} can be found by numerically integrating the time-averaged intensity through the plate cross-section:

$$P_{x0} = \int_{-h}^{h} I_x(y)\mathrm{d}y = -\frac{1}{2}\int_{-h}^{h} \mathrm{Re}\left\{v_x(y)\overline{\sigma_{xx}}(y) + v_y(y)\overline{\sigma_{xy}}(y)\right\}\mathrm{d}y. \tag{28}$$

For a *leaky* antisymmetric Lamb wave in a plate of density ρ_p immersed in a fluid of density ρ_f, a tractable and exact extension to the characteristic equation in Eq. (25) can be found in the literature [1,18,35,39,40]:

$$\frac{\tan(\gamma_\mathrm{P} h)}{\tan(\gamma_\mathrm{S} h)} + \frac{4k_x^2\gamma_\mathrm{S}\gamma_\mathrm{P}}{(k_x^2 - \gamma_\mathrm{S}^2)^2} = -i\frac{\rho_\mathrm{f}\omega^4\gamma_\mathrm{P}}{\rho_\mathrm{p}c_\mathrm{S}^4 k_y(k_x^2 - \gamma_\mathrm{S}^2)^2}\cdot\frac{1}{\tan(\gamma_\mathrm{S} h)}. \tag{29}$$

This leaky-wave characteristic equation is more difficult to solve than the free-wave characteristic equation, Eq. (25). While the characteristic equation for free waves only needs to be solved for a real-valued k_x for each frequency ω, the characteristic equation for leaky waves must be solved simultaneously for the real and imaginary components $k_{x\mathrm{r}}$ and $k_{x\mathrm{i}}$.

5.2. Method

We focus on four combinations of materials, specifically plates of steel and brass immersed in air and water, with material parameters specified in Table 1. For a given plate thickness $d = 1$ cm, we begin by calculating the wavenumbers that satisfy the A_0 dispersion relation near coincidence. From Eq. (25) we obtain the real-valued free-wave wavenumber k_x^free, whereas Eq. (29) yields the complex leaky-wave wavenumber k_x^leaky.

To evaluate the radiation model in Eq. (18) as a perturbation method, we will compare the exact attenuation $k_{x\mathrm{i}}^\mathrm{leaky}$ with the attenuation $k_{x\mathrm{i}}$ found by three perturbation approaches:

1. Neglecting the effect of vibrational attenuation and hence getting *homogeneous* radiated waves, we calculate the classical perturbation solution $k_{x\mathrm{i}}^\mathrm{hom}$ [18–20] via k_x^free following Eq. (19).
2. Including the effect of vibrational attenuation that causes the radiated waves to become *inhomogeneous*, we calculate the attenuation $k_{x\mathrm{i}}$ via k_x^free by solving the radiation model in Eq. (18).
3. Again including vibrational attenuation, we calculate the attenuation $k_{x\mathrm{i}}$ using Eq. (18), but via $k_{x\mathrm{r}}^\mathrm{leaky}$, the dispersion of the *exact* solution.

In all three cases, we determine the radiated intensity and power flow via the wavefield expressions in Eq. (27), keeping in mind that the total radiated intensity is twice that of Eq. (14a) because Lamb waves radiate power on both sides of the plate.

These three approaches are chosen to highlight the effect of including additional information in the perturbation method. First, by including the effect of vibrational attenuation and the resulting inhomogeneity, and second, by including the exact dispersion. However, we point out that the third approach would not have much practical value as it estimates the attenuation using the real part of the exact wavenumber k_x^leaky, whose imaginary part already contains the exact attenuation.

To summarise, our perturbation method approach for each material combination is as follows. At each frequency f, we first calculate the free-plate wavenumber k_x^free and the exact leaky wavenumber k_x^leaky from Eqs. (25) and (29), respectively. Using the real parts of these wavenumbers and an assumed value of $k_{x\mathrm{i}}$, we can calculate the velocity and stress wavefields from Eq. (27), and subsequently the power flow amplitude P_{x0} from Eq. (28). These let us calculate the approximate attenuation $k_{x\mathrm{i}}$, either explicitly from Eq. (19) (assuming $k_{x\mathrm{i}} \approx 0$ in Eq. (27)) or iteratively from Eq. (18), which takes wave inhomogeneity and energy conservation into account, but which also requires recalculating $|v_{y0}|$ and P_{x0} in each iteration using that iteration's value of $k_{x\mathrm{i}}$.

To validate the radiation model in Eq. (18) against the exact Lamb wave solution, we can use k_x^leaky to directly calculate the exact values of $|v_{y0}|$ and P_{x0} and insert these into Eq. (18) to check that these values correspond to a root. To obtain exact leaky wavefields from Eq. (27), we must also tune the free-plate amplitude ratio R^A to correspond to an immersed plate. This can be

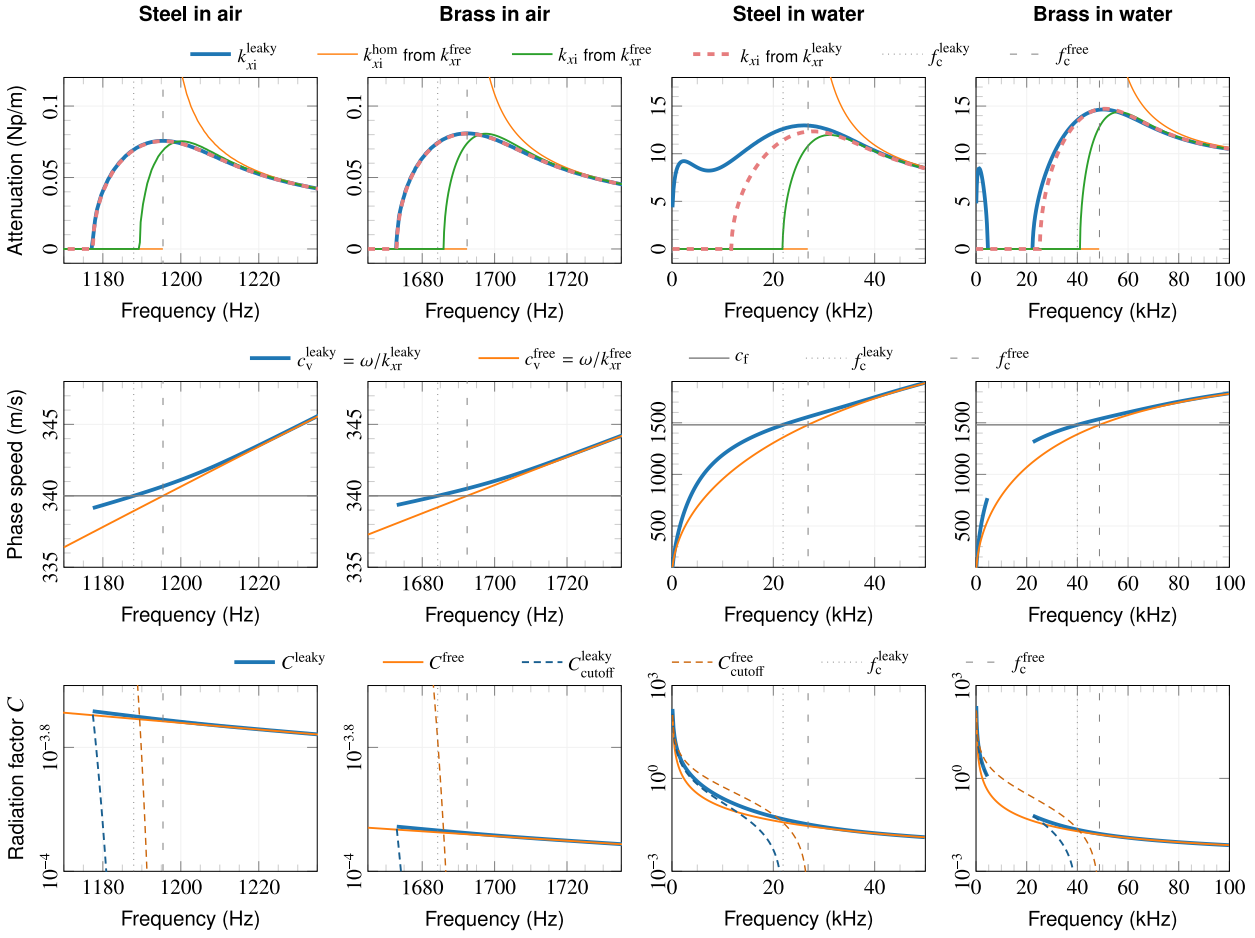

Fig. 11. Various leaky A_0 Lamb wave properties (rows) for different material combinations (columns) of a 1 cm thick plate immersed in a fluid. Where k_{xi}^{leaky} reaches 0 at low frequencies, the exact leaky A_0 wave is cut off as it splits into a loop of two different lossless waves [9–12,33], not shown here. For brass in water, this loop closes at very low frequencies to become a leaky A_0 wave again [9,11,12,14,33].

straightforwardly achieved by optimising R^{A} against a cost function corresponding to the wavefields' deviations from the general boundary conditions

$$\sigma_{xy}(y=\pm h)=0, \qquad \sigma_{yy}(y=\pm h)=-p(y=\pm h)=-\rho\omega v_y(y=\pm h)/(\pm k_y), \tag{30}$$

giving the amplitude ratio $R^{\text{A,leaky}}$ for an immersed plate. The last equality in Eq. (30) follows from Eq. (11b).

5.3. Results

Fig. 11 shows various leaky Lamb wave properties for each of the chosen combinations of materials close to the classical coincidence frequency $f_{\text{c}}^{\text{free}}$. The top row compares the exact attenuation k_{xi}^{leaky} with the attenuations found by the three perturbation approaches explained in Section 5.2. Let us consider how these attenuations evolve from high to low frequencies. At high frequencies, well into the classical supersonic domain, the different attenuation estimates converge with the exact attenuation k_{xi}^{leaky}. As we approach the coincidence frequency $f_{\text{c}}^{\text{free}}$, however, differences emerge. As we saw previously in Fig. 8, the attenuation k_{xi}^{hom} of the classic perturbation method, which assumes homogeneous waves, rises and reaches an infinite discontinuity at the coincidence frequency $f_{\text{c}}^{\text{free}}$, while predicting no radiation in the subsonic domain. The attenuation k_{xi} predicted by the inhomogeneous-wave perturbation method based on k_{xr}^{free} follows the exact attenuation more closely towards coincidence and predicts subsonic radiation *qualitatively* but not *quantitatively* correctly; it peaks and cuts off at higher frequencies than the exact attenuation.

The main reason for this peak and cutoff mismatch can be seen in the phase speed results on the middle row of Fig. 11. At high frequencies, the speeds of the free and leaky Lamb waves converge, but these speeds diverge as we approach coincidence, as others have also remarked [10,12,33]. The leaky Lamb waves' higher phase speed near coincidence leads to a lower coincidence frequency $f_{\text{c}}^{\text{leaky}} < f_{\text{c}}^{\text{free}}$. This explains most of the discrepancy between the exact attenuation and the inhomogeneous attenuation calculated via k_{xr}^{free}: we see from the top row that the inhomogeneous attenuation k_{xi} calculated via k_{xr}^{leaky} gives an excellent match with the

exact attenuation for solid plates in air, and a good match for brass in water except at very low frequencies where the A_0 wave reappears, an effect that has been seen throughout the literature [9,12,14,33].

For the plates in water, in particular the steel plate, we still see a clear discrepancy even when using k_{xr}^{leaky} as a basis for calculating the inhomogeneous attenuation via the radiation model in Eq. (18). The remaining known source of error is the usage of the free-plate value of R^{A} from Eq. (27f), which means that the wavefields calculated from Eq. (27) do not perfectly respect the exact boundary conditions in Eq. (30). By substituting the immersed-plate value $R^{\text{A,leaky}}$, found as described in Section 5.2, we can calculate accurate wavefields for a leaky Lamb wave from Eq. (27), from which we can determine $|v_{y0}|$ and P_{x0}.

The resulting attenuation curves found from the radiation model have a perfect visual match with the k_{xi}^{leaky} curves and were therefore not plotted separately in Fig. 11. Instead, we can investigate the match quantitatively to validate the correctness of radiation model equation Eq. (18) for these four cases. As $f(k_{xr}, k_{xi})$ represents the model's signed error in k_{xi}, inputting exact leaky-wave values for k_{xr}, k_{xi}, v_{y0} and P_{x0} will give $f = 0$ if the model is correct. Moreover, we can calculate the relative error as

$$\left|\frac{f(k_{xr}^{\text{leaky}}, k_{xi}^{\text{leaky}})}{k_{xi}^{\text{leaky}}}\right| = \left|1 - \frac{k_{yr}^{\text{leaky}}}{\left|k_y^{\text{leaky}}\right|^2}\frac{\rho\omega|v_{y0}|^2}{2P_{x0}k_{xi}^{\text{leaky}}}\right|, \tag{31}$$

where k_y^{leaky} is calculated using k_x^{leaky} in Eq. (10). Across the various combinations of materials and frequencies shown in Fig. 11, the maximum relative error is 8.6×10^{-9}. We can safely attribute this minuscule deviation to the accumulation of tiny numerical errors when calculating the exact leaky Lamb wave quantities. (Indeed, the relative error is sensitive to the tolerances chosen when calculating k_x^{leaky} and $R^{\text{A,leaky}}$ and the spatial sampling density chosen for the plate cross-section when calculating P_{x0}.) Thus, the radiation model in Eq. (18) is found to match an exact (to a very good numerical precision) leaky Lamb wave solution, which along with the results of [13] supports the hypothesis of Section 4.1, namely that the radiation model is a correct description of sound radiation.[4]

Finally, we consider the bottom row of Fig. 11. These plots show how the radiation factors of Eq. (20) evolve with frequency close to coincidence. (While we kept C constant for simplicity in Section 4, C will vary in a Lamb wave because k, $|v_{y0}|$, and P_{x0} change with the frequency.) We calculated C^{free} via k_x^{free} and R^{A}, and C^{leaky} via k_x^{leaky} and $R^{\text{A,leaky}}$. For the plates in air, the variations in C are quite small in the plotted range, and C itself is so small that subsonic radiation is only possible in a very small interval below coincidence, as per the radiating wave cutoff results of Eq. (21) and Fig. 9a. For the plates in water, however, the C values near coincidence are higher, which lets the subsonic radiation extend further down into the low frequencies. Then, as we go down in frequency, C starts increasing rapidly, which as per Fig. 9a pushes the wave's cutoff lower and lower in frequency. In other words, the cutoff becomes a "moving target" that the subsonic radiation for brass in water reaches, but which the subsonic radiation for steel in water does not reach (and never will, according to [11]).

This effect becomes more apparent if we compare the evolution of C with the value of C that would correspond to a subsonic wave cutoff for the current relative phase speed c_v/c_f. Replacing C with $2C$ in Eq. (21) to take into account the radiation from both sides of the plate, we find this cutoff value to be exactly

$$C_{\text{cutoff}} = \frac{1}{2}\frac{[(c_f/c_v)^2 - 1]^{3/2}}{c_f/c_v}. \tag{32}$$

Cutoff curves $C_{\text{cutoff}}^{\text{leaky}}$ and $C_{\text{cutoff}}^{\text{free}}$, calculated respectively from c_v^{leaky} and c_v^{free}, are plotted in the bottom row of Fig. 11. As expected, the crossing frequencies of C and C_{cutoff} correspond to the cutoff frequencies of the subsonic radiating wave. For the case of brass in water, $C_{\text{cutoff}}^{\text{leaky}}$ catches up to C^{leaky} soon after coincidence, while for the case of steel in water, C^{leaky} increases quickly enough at low frequencies that $C_{\text{cutoff}}^{\text{leaky}}$ does not catch up. For that reason, the subsonic radiation of steel in water manages to extend into very low frequencies without cutting off.

6. Discussion

First, let us analyse the radiation model from Section 4 to identify *why* it permits subsonic radiation. Essentially, the radiation model is a simple statement of energy conservation that equates the radiated intensity with the power loss in the guided wave underlying the surface vibration. The key quantity is the attenuation k_{xi}: according to Eq. (16), $2k_{xi}$ is the relative power loss in Np/m, and according to Eq. (14a) and Fig. 6a, the radiated intensity amplitude $I_{\text{rad},0}$ is a nonlinear function of k_{xi} via k_y. The intensity vector magnitude $|\mathbf{I}_0| = \rho\omega|\mathbf{k}_r||v_{y0}|^2/2|k_y|^2$ from Eq. (12) is largely only weakly affected by k_{xi} through $|k_y|^2$, except very near coincidence where Eq. (A.5) shows that $|k_y|^2 \approx 2k_{xi}k$. Hence, the main effect of k_{xi} on the intensity is moving the direction of the intensity vector $\mathbf{I}_0$ up from a grazing angle and into the fluid, as seen in Fig. 6b, thus increasing the radiated intensity $I_{\text{rad},0} = I_{y0}$.

According to the radiation model in Eq. (18), a wave solution exists when the relative power loss $2k_{xi}$ equals the relative radiated intensity $I_{\text{rad},0}/P_{x0}$. In the subsonic domain, this is trivially satisfied for $k_{xi} = 0$, describing an evanescent wave with no power loss and no radiation. However, for a value of c_v/c_f where subsonic radiation is possible, the sign of the surface plots in Fig. 8 shows that the relative intensity $I_{\text{rad},0}/P_{x0}$ first grows more quickly than the power loss $2k_{xi}$ as k_{xi} increases from 0, and then more slowly.

[4] While this validation covers the various subsonic A_0 wave behaviours observed for the most typical case of $c_f < c_R$ (c_R being the Rayleigh wave speed), different but related subsonic behaviours of multiple leaky Lamb waves emerge when $c_R < c_f$ [11,27,41]. However, the generality of the derivation of the radiation model means that there is no specific reason to doubt its validity for those other subsonic cases.

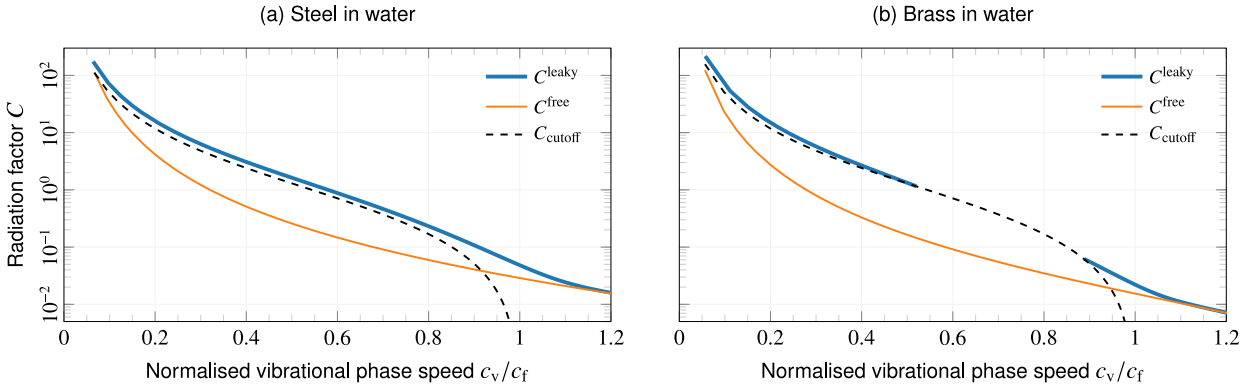

Fig. 12. Radiation factors for leaky A_0 Lamb waves on immersed plates in water.

The wave solution exists at the point where power loss catches up to the relative intensity, such that energy is conserved. For a value of c_v/c_f where subsonic radiation is *not* possible, however, Fig. 8 shows that the relative intensity *always* grows more slowly than the power loss. In other words, while increasing k_{xi} increases the radiated intensity by changing the direction of the intensity vector, the power loss is increased even more quickly, and there exists no positive value of k_{xi} for which energy is conserved.

Many earlier sources have incorrectly implied that subsonic radiation from surface vibrations is impossible, for various reasons. Some sources have not taken into account the attenuation of the surface vibration, a choice that disregards conservation of energy and does not lead to inhomogeneous radiated waves. Others end up incorrectly rejecting the correct solution because it describes a pressure amplitude that goes to infinity with the distance to the surface. As we and others [13,15,27,32] have explained, this is actually a necessary property of all unbounded leaky forward waves.

Testing the radiation model against Lamb waves in Section 5 led to several interesting results. First, our findings support the correctness of the radiation model, as we found the exact leaky Lamb wave solution to be a root of the radiation model in Eq. (18). In other words, we have found that subsonic radiation is possible because of the inhomogeneity of the radiated wave, which is caused by the attenuation of the surface vibration due to the loss of the power radiated into the fluid.

As for using the radiation model as a basis for a perturbation method based on the free Lamb wave solution, the results are mixed, because the neglected effects of fluid loading on the dispersion and wavefields of the Lamb wave turn out to be quite important close to coincidence. While the model's attenuation prediction is certainly better than that of existing perturbation methods close to coincidence – it avoids the infinite discontinuity at coincidence, predicts subsonic radiation, and approximates the maximum attenuation well – it is unable to fully predict the subsonic shape of the radiating wave. For plates in air, getting a good match requires using the exact dispersion k_{xr}^{leaky} to take into account the additional dispersion near coincidence caused by the fluid loading. For plates in water, changes of the wavefields in the plate also need to be considered, because the mismatch between the free-plate boundary conditions and the true boundary conditions becomes too strong otherwise.

Furthermore, the resulting perturbation method involves solving Eq. (18) iteratively, which negates some of the benefit of using a perturbation method based on the free-plate solution instead of directly finding the exact solution. Thus, while using a perturbation method based on the enhanced radiation model may give some benefit close to coincidence, using existing perturbation methods is more expedient well into the supersonic domain, which for light fluid loading typically encompasses every Lamb mode except for A_0 at low frequencies, as we can see from Fig. 10.

When applied to the exact solution for a fluid-loaded plate, though, the radiation model may help provide a physical explanation of some of the more peculiar subsonic behaviours that have been observed in the literature, such as the persistence of subsonic radiating waves [10,11,13], which we saw for the steel-in-water wave in Fig. 11, and the reappearance of a leaky A_0 wave at very low frequencies below its initial cutoff [9–12,14], which we saw for the brass-in-water wave in Fig. 11. Fig. 12 plots the radiation factors C for these two cases against c_v/c_f. From this, we can see more clearly than from Fig. 11 how the leaky steel-in-water wave just barely avoids being cut off from $c_v/c_f \approx 0.8$ and down, explaining its persistence. Fig. 12 also shows how the brass-in-water wave, with its slightly lower value of C^{leaky}, *does* get cut off at $c_v/c_f \approx 0.89$, at which point the radiation model in Eq. (18) shows that an energy-conserving radiating subsonic A_0 wave is no longer possible. This triggers the A_0 wave to be split into a loop of two non-radiating waves. (Such loops have been shown in many references [9–13,33,41]; in particular, Shuvalov et al. [11] carried out a detailed mathematical analysis of the loops.) At $c_v/c_f \approx 0.52$, the loop closes again as an energy-conserving radiating A_0 wave again becomes possible.

The brass-in-water results of Fig. 12 also help provide a physical explanation for the results of Dabirikhah and Turner [10], who calculated the attenuation of a leaky A_0 Lamb wave in an aluminium plate immersed in air, while gradually increasing the air density. At normal air densities, they found that the subsonically radiating A_0 wave only exists slightly below coincidence. At higher densities, they found that not only does the attenuation increase, the wave also reappears at low frequencies like we saw for brass in water. At the highest investigated density, they found the radiating wave to persist into low frequencies like the steel-in-water

wave in Fig. 11. From Eq. (20), we find that because C is proportional to density, reducing the fluid density would shift C down in Fig. 12b, so that the subsonic radiation would cut off just below coincidence. Increasing the fluid density would shift C up, which would lead to the subsonic radiation persisting without cutoff, similarly to the steel-in-water wave in Fig. 11.

Finally, we point out a puzzling consequence of our result from Section 3 that *all* attenuated surface vibrations will lead to a radiating wave. Because lossless materials exist only in theory, any real material will have some amount of loss that would lead to a small attenuation of any kind of surface vibration on the material. This implies that classical evanescent waves like that shown in Fig. 1c cannot in fact exist in the real world, because we showed in Section 3 that evanescent waves can only arise from *unattenuated* surface vibrations. However, a closer investigation of this topic is beyond the scope of this article.

7. Conclusion

In this work, we have shown how a comprehensible model for how surface vibrations radiate pressure waves into an adjacent fluid can be straightforwardly derived. This model is general, not tied to a specific type of leaky guided wave such as leaky Lamb waves or leaky Rayleigh waves (although our analysis of the model was limited to forward waves). Unlike the classical model, this model takes into account the attenuation of the surface vibration and the resulting inhomogeneity of the pressure wave, which permits power radiation into the fluid even in the subsonic domain. It also respects conservation of energy by equating the power radiated by the pressure wave in the fluid with the power lost in the surface vibration. Subsonic radiation can occur in a subsonic subdomain close to coincidence where this power balance is possible.

In Section 4, we posed the hypothesis that this model correctly describes the mechanism underlying subsonic radiation. The leaky A_0 Lamb wave results of Section 5 support this hypothesis, as the exact leaky Lamb wave solves Eq. (18), the equation at the heart of the radiation model.

When applying the radiation model as a perturbation method to predict the attenuation of leaky A_0 Lamb waves from the properties of free A_0 waves, we found that it performed somewhat better than existing perturbation methods by predicting a finite attenuation at coincidence, predicting the existence of subsonic radiation, and approximating the maximum attenuation well. However, it does not correctly predict the shape of the attenuation curve close to coincidence, because doing so requires taking into account the full effects of fluid loading on the Lamb wave. Even so, the model was able to shed light on the surprising differences in the leaky A_0 wave cutoff across different combinations of materials. These differences are mainly due to the sound radiation instead of internal behaviour of the Lamb wave; when energy-conserving subsonic radiation is no longer possible, the radiating A_0 wave cuts off. In some cases, such as brass in water, the A_0 wave may even return at low frequencies when it again becomes possible.

One particularly important piece of future work is to extend this radiation model to the case of surface vibrations radiating into solids. In fact, we have already published a preliminary investigation into this topic [42]. As solids carry both P- and S-waves, which have different speeds of sound c_P and c_S, we go from two radiation domains for fluids (namely, $c_f < c_v$ and $c_v < c_f$) to three radiation domains (namely, $c_S < c_P < c_v$, $c_S < c_v < c_P$, and $c_v < c_S < c_P$). Because the transition between these domains is essential to measurement techniques in, e.g., ultrasonic pitch-catch well logging [43,44], a better physical understanding of what happens around these transitions should facilitate improvements to such techniques.

CRediT authorship contribution statement

Erlend Magnus Viggen: Conceptualization, Methodology, Software, Validation, Formal analysis, Writing – original draft, Writing – review & editing, Visualization. **Håvard Kjellmo Arnestad:** Conceptualization, Methodology, Software, Formal analysis, Writing – original draft, Writing – review & editing.

Declaration of competing interest

The authors declare that they have no known competing financial interests or personal relationships that could have appeared to influence the work reported in this paper.

Data availability

No data was used for the research described in the article.

Acknowledgements

The authors thank Sven Peter Näsholm (University of Oslo) and U. Peter Svensson (Norwegian University of Science and Technology) for reading and commenting on a draft version of this article. The authors also wish to thank an anonymous reviewer for his or her uncommonly insightful and thorough comments. This work was supported by the Research Council of Norway [grant number 237887].

Appendix. Calculating characteristics of the radiating wave

From the normalised radiation model in Eq. (20), we can determine various characteristics of the radiating forward wave. As the calculations become somewhat involved, we start by simplifying the notation of Eq. (20) as

$$k_{x\mathrm{r}}/k = x \in \mathbb{R}_{\geq 0}, \qquad k_{x\mathrm{i}}/k = y \in \mathbb{R}_{\geq 0}, \qquad k_y/k = z(x,y) = \sqrt{1-(x+\mathrm{i}y)^2} \in \mathbb{C}, \tag{A.1}$$

$$g(x,y,C) = y - \frac{z_\mathrm{r}}{|z|^2}C = 0, \tag{A.2}$$

where $C \in \mathbb{R}_{\geq 0}$, and $z_\mathrm{r} \in \mathbb{R}_{\geq 0}$ is the real part of z. We can view y as an implicit function $y(x,C)$, defined by the implicit equation Eq. (A.2).

A.1. Cutoff of the subsonic radiating wave

Fig. 8 shows that for higher C values, the radiating waves extend further into the subsonic domain before they are cut off. This cutoff point x_cutoff can be specified exactly from the limit $\lim_{y\to 0^+} g(x_\mathrm{cutoff}, y, C) = 0$ in the subsonic domain ($x > 1$). We can derive an expression for it via Taylor expanding $g(x,y,C) = 0$ around $y = 0$ using a computer algebra system. The $\mathcal{O}(1)$ term in the Taylor series is always zero in the subsonic domain — it corresponds to the root at $y = 0$ representing an evanescent wave. Thus, the lowest-order nonzero term is the $\mathcal{O}(y)$ term, and higher-order terms can be neglected in the $y \to 0^+$ limit. Taking this limit in the $\mathcal{O}(y)$ term, simplifying it, and solving for x leads to an exact implicit equation for the subsonic cutoff point:

$$\frac{[x_\mathrm{cutoff}^2 - 1]^{3/2}}{x_\mathrm{cutoff}} = C. \tag{A.3}$$

Solutions of this implicit equation can be found numerically using a root-finding algorithm, which gives the same results as the contour-finding algorithm used to draw the roots in Fig. 8.

We can also find an explicit approximation of this solution by taking the first term of a Puiseux series of the left-hand side of Eq. (A.3) around $x_\mathrm{cutoff} = 1$:

$$2^{3/2}\left(x_\mathrm{cutoff} - 1\right)^{3/2} \approx C \quad \Rightarrow \quad x_\mathrm{cutoff} \approx 1 + \frac{C^{2/3}}{2}. \tag{A.4}$$

A.2. Attenuation at coincidence

At coincidence ($x = 1$), we get a significantly simpler expression for $z = k_y/k$, which can be approximated in the limits of low and high y:

$$z(x=1,y) = \sqrt{y^2 - 2\mathrm{i}y} \approx \begin{cases} \sqrt{y}(1-\mathrm{i}) & \Rightarrow \quad z_\mathrm{r} \approx \sqrt{y}, \quad |z|^2 \approx 2y \quad \text{for } y \ll 1, \\ y & \Rightarrow \quad z_\mathrm{r} \approx y, \quad |z|^2 \approx y^2 \quad \text{for } y \gg 1. \end{cases} \tag{A.5}$$

Inserting these results into Eq. (A.2), we find $y = k_{x\mathrm{i}}/k$ at coincidence to be approximately:

$$y(x=1,C) \approx \begin{cases} \dfrac{1}{2\sqrt{y(x=1,C)}}C \approx \left(\dfrac{C}{2}\right)^{2/3} & \text{for } y \ll 1, \\ \dfrac{1}{y(x=1,C)}C \approx \sqrt{C} & \text{for } y \gg 1. \end{cases} \tag{A.6}$$

These results show that these two limits can equivalently be expressed as $C \ll 1$ and $C \gg 1$, respectively.

A.3. Peak coordinates

From Fig. 8, we see that the attenuation of the radiating wave peaks close to coincidence in the supersonic domain. For larger C, the peak is taller and further away from coincidence. At $C \approx 0.866$, the nature of the radiating wave's attenuation curve changes, so that there is no longer a local maximum in $y(x,C)$; it becomes monotonic in x. For that reason, we only perform this investigation for lower values of C.

While this peak can be defined by $\mathrm{d}y(x,C)/\mathrm{d}x = 0$, we were unable to find even an approximate analytical expression by means of implicit differentiation, Lagrange multipliers, or series expansion around $x = 1$, $y = 0$. However, finding the peaks numerically is straightforward. We can find the radiating wave's attenuation $y(x,C)$ in the supersonic domain as the root of $g(x,y,C) = 0$. By varying x, we can identify the peak in $y(x,C)$ and determine the peak coordinate $(x_\mathrm{peak}(C), y_\mathrm{peak}(C))$ to the desired numerical precision. We can then find approximate functions in C for these coordinates by means of curve fitting. As we want to find the peak's normalised vibrational phase speed $c_{\mathrm{f,peak}}/c_\mathrm{f} = 1/x_\mathrm{peak}$ in the end, which goes to 1^+ as $C \to 0^+$, we will look for a fit to $1/x_\mathrm{peak} - 1$.

Starting with very small values $C \in [10^{-6}, 10^{-5}]$ to approximately find the lowest term of a series expansion in C, we find that

$$\lim_{C\to 0^+}\left[\frac{1}{x_\mathrm{peak}(C)} - 1\right] = \frac{C^{2/3}}{b_x}, \qquad \lim_{C\to 0^+} y_\mathrm{peak}(C) = \frac{C^{2/3}}{b_y}. \tag{A.7}$$

Iterative analysis of the remainder for higher values of C reveals higher-order terms in $C^{4/3}$, $C^{6/3}$, and so forth. However, in order to achieve a good fit with fewer constants, we fit functions on the form

$$\frac{1}{x_{\text{peak}}(C)} - 1 \approx \frac{1}{a_x + b_x C^{-2/3}}, \qquad y_{\text{peak}}(C) \approx \frac{1}{a_y + b_y C^{-2/3}}, \tag{A.8}$$

whose lowest-order terms in a series expansion in C equal Eq. (A.7). The higher-order terms in this series expansion are in the same powers of C as we found in our remainder analysis.

To ensure that the curve fitted function is good both for very small values of C and for higher values of C, we perform least-squares curve fitting in two steps. First, we determine b_x and b_y by fitting functions on the form Eq. (A.7) to peaks found for $C \in [10^{-6}, 10^{-5}]$. Second, we hold these values of b_x and b_y constant and determine a_x and a_y by curve fitting functions on the form Eq. (A.8) to peaks found for $C \in [10^{-3}, 10^{-1}]$. The resulting values are

$$a_x = -2.0919058, \qquad b_x = 2.5193662, \qquad a_y = -0.19195482, \qquad b_y = 1.4547858. \tag{A.9}$$

A.4. Asymptotic supersonic attenuation

We can find the asymptotic value of the attenuation in the supersonic domain by letting $x = c_f/c_v \to 0$, where

$$z(x = 0, y) = \sqrt{1 + y^2}, \qquad \text{and} \qquad g(x = 0, y, C) = y - \frac{C}{\sqrt{1 + y^2}} = 0. \tag{A.10}$$

The latter equation has four roots of y, one of which is real-valued and positive:

$$y(x = 0, C) = \sqrt{\frac{\sqrt{1 + 4C^2} - 1}{2}} \approx \begin{cases} C & \text{for } C \ll 1, \\ \sqrt{C} & \text{for } C \gg 1. \end{cases} \tag{A.11}$$

For low values of C, $y(x = 0, C) \approx C$.

References

[1] I.A. Viktorov, Rayleigh and Lamb Waves: Physical Theory and Applications, first ed., Plenum Press, New York, NY, 1967.
[2] P.M. Morse, K.U. Ingard, Theoretical Acoustics, McGraw-Hill, 1968.
[3] N. Brower, D. Himberger, W. Mayer, Restrictions on the existence of leaky Rayleigh waves, IEEE Trans. Sonics Ultrason. 26 (4) (1979) 306–307, http://dx.doi.org/10.1109/T-SU.1979.31104.
[4] L.M. Brekhovskikh, O.A. Godin, Acoustics of Layered Media I, first ed., in: Springer Series on Wave Phenomena, vol. 5, Springer-Verlag Berlin Heidelberg, 1990, http://dx.doi.org/10.1007/978-3-642-52369-4.
[5] G. Williams, Fourier Acoustics: Sound Radiation and Nearfield Acoustical Holography, Elsevier Science, 1999.
[6] L. Cremer, M. Heckl, B.A.T. Petersson, Structure-Borne Sound, third ed., Springer, 2005.
[7] T.E. Vigran, Building Acoustics, CRC Press, 2008.
[8] A.D. Pierce, Acoustics, third ed., Springer Nature Switzerland AG, 2019.
[9] H. Dabirikhah, C. Turner, Anomalous behaviour of flexural waves in very thin immersed plates, in: Proceedings of the IEEE 1992 Ultrasonics Symposium, IEEE, Tucson, AZ, USA, 1992, pp. 313–317, http://dx.doi.org/10.1109/ULTSYM.1992.275989.
[10] H. Dabirikhah, C.W. Turner, The coupling of the A_0 and interface Scholte modes in fluid-loaded plates, J. Acoust. Soc. Am. 100 (5) (1996) 3442–3445, http://dx.doi.org/10.1121/1.416985.
[11] A. Shuvalov, O. Poncelet, M. Deschamps, Analysis of the dispersion spectrum of fluid-loaded anisotropic plates: Flexural-type branches and real-valued loops, J. Sound Vib. 290 (3–5) (2006) 1175–1201, http://dx.doi.org/10.1016/j.jsv.2005.05.015.
[12] D.A. Kiefer, M. Ponschab, S.J. Rupitsch, M. Mayle, Calculating the full leaky Lamb wave spectrum with exact fluid interaction, J. Acoust. Soc. Am. 145 (6) (2019) 3341–3350, http://dx.doi.org/10.1121/1.5109399.
[13] D.A. Kiefer, M. Ponschab, S.J. Rupitsch, From Lamb waves to quasi-guided waves: On the wave field and radiation of elastic and viscoelastic plates, 2020, http://dx.doi.org/10.13140/RG.2.2.32631.44968, Preprint on ResearchGate.
[14] E. Ducasse, M. Deschamps, Mode computation of immersed multilayer plates by solving an eigenvalue problem, Wave Motion 112 (2022) 102962, http://dx.doi.org/10.1016/j.wavemoti.2022.102962.
[15] V. Mozhaev, M. Weihnacht, Subsonic leaky Rayleigh waves at liquid–solid interfaces, Ultrasonics 40 (1–8) (2002) 927–933, http://dx.doi.org/10.1016/S0041-624X(02)00233-0.
[16] N.D. Sandham, C.L. Morfey, Z.W. Hu, Sound radiation from exponentially growing and decaying surface waves, J. Sound Vib. 294 (1–2) (2006) 355–361, http://dx.doi.org/10.1016/j.jsv.2005.10.012.
[17] N. Declercq, R. Briers, J. Degrieck, O. Leroy, The history and properties of ultrasonic inhomogeneous waves, IEEE Trans. Ultrason. Ferroelectr. Freq. Control 52 (5) (2005) 776–791, http://dx.doi.org/10.1109/TUFFC.2005.1503963.
[18] L.G. Merkulov, Damping of normal modes in a plate immersed in a liquid, Sov. Phys.: Acoust. 10 (2) (1964) 169–173.
[19] B.A. Auld, Acoustic Fields and Waves in Solids, Vol. 2, first ed., John Wiley & Sons, 1973.
[20] R. Watkins, W. Cooper, A. Gillespie, R. Pike, The attenuation of Lamb waves in the presence of a fluid, Ultrasonics 20 (6) (1982) 257–264, http://dx.doi.org/10.1016/0041-624X(82)90046-4.
[21] H.K. Arnestad, E.M. Viggen, A fast semi-analytical method for propagating leaky Lamb wavefields, in: Proceedings of the 44th Scandinavian Symposium on Physical Acoustics, Norwegian Physical Society, Online, 2021, p. 23.
[22] H.K. Arnestad, A Fast Simulation Method for Ultrasonic Wave Propagation in Coupled Non-Parallel Plates — With Applications to Inversion of Pitch-Catch through-Tubing Well Logging (Master's thesis), Norwegian University of Science and Technology, 2021.
[23] E.M. Viggen, H.K. Arnestad, Understanding sound radiation from surface vibrations moving at subsonic speeds, in: Proceedings of the 44th Scandinavian Symposium on Physical Acoustics, Norwegian Physical Society, Online, 2021, p. 4, Extended abstract.
[24] I. Tolstoy, E. Usdin, Wave propagation in elastic plates: Low and high mode dispersion, J. Acoust. Soc. Am. 29 (1) (1957) 37–42, http://dx.doi.org/10.1121/1.1908675.

[25] J. Wolf, T.D.K. Ngoc, R. Kille, W.G. Mayer, Investigation of Lamb waves having a negative group velocity, J. Acoust. Soc. Am. 83 (1988) 122–126, http://dx.doi.org/10.1121/1.396438.
[26] C. Prada, D. Clorennec, D. Royer, Local vibration of an elastic plate and zero-group velocity Lamb modes, J. Acoust. Soc. Am. 124 (1) (2008) 203–212, http://dx.doi.org/10.1121/1.2918543.
[27] D.A. Kiefer, Elastodynamic Quasi-Guided Waves for Transit-Time Ultrasonic Flow Metering (Ph.D. thesis), Friedrich-Alexander-Universität Erlangen-Nürnberg, 2022, p. 213, http://dx.doi.org/10.25593/978-3-96147-550-6.
[28] R.D. Borcherdt, L. Wennerberg, General P, Type-I S, and Type-II S waves in anelastic solids; Inhomogeneous wave fields in low-loss solids, Bull. Seismol. Soc. Am. 75 (6) (1985) 1729–1763.
[29] B. Poirée, Complex harmonic plane waves, in: O. Leroy, M.A. Breazeale (Eds.), Physical Acoustics: Fundamentals and Applications, Springer US, Boston, MA, 1991, pp. 99–117, http://dx.doi.org/10.1007/978-1-4615-9573-1_10.
[30] N. Marcuvitz, On field representations in terms of leaky modes or Eigenmodes, IRE Trans. Antennas Propag. 4 (3) (1956) 192–194, http://dx.doi.org/10.1109/TAP.1956.1144410.
[31] J. Hu, C.R. Menyuk, Understanding leaky modes: Slab waveguide revisited, Adv. Opt. Photonics 1 (1) (2009) 58, http://dx.doi.org/10.1364/AOP.1.000058.
[32] E. Georgiades, M.J.S. Lowe, R.V. Craster, Leaky wave characterisation using spectral methods, 2022, http://dx.doi.org/10.48550/arXiv.2206.06977, Preprint arXiv:2206.06977.
[33] A. Freedman, Anomalies of the A_0 leaky Lamb mode of a fluid-loaded, elastic plate, J. Sound Vib. 183 (4) (1995) 719–737, http://dx.doi.org/10.1006/jsvi.1995.0282.
[34] J. Rose, Ultrasonic Guided Waves in Solid Media, Cambridge University Press, 2014.
[35] M. Lowe, B. Pavlakovic, DISPERSE User's Manual v2.0.20a, Department of Mechanical Engineering, Imperial College London, 2013.
[36] M. Lowe, Matrix techniques for modeling ultrasonic waves in multilayered media, IEEE Trans. Ultrason. Ferroelectr. Freq. Control 42 (4) (1995) 525–542.
[37] V. Giurgiutiu, Structural Health Monitoring with Piezoelectric Wafer Active Sensors, second ed., Academic Press, 2014.
[38] A.M. Kamal, B. Lin, V. Giurgiutiu, Exact analytical modeling of power and energy for multimode lamb waves excited by piezoelectric wafer active sensors, J. Intell. Mater. Syst. Struct. 25 (4) (2014) 452–471.
[39] M.F.M. Osborne, S.D. Hart, Transmission, reflection, and guiding of an exponential pulse by a steel plate in water. I. Theory, J. Acoust. Soc. Am. 17 (1) (1945) 1–18, http://dx.doi.org/10.1121/1.1916293.
[40] A. Schoch, Der schalldurchgang durch platten [The transmission of sound through plates], Acustica 2 (1) (1952) 1–17.
[41] K. van de Rostyne, C. Glorieux, W. Gao, W. Lauriks, J. Thoen, Experimental investigation of leaky Lamb modes by an optically induced grating, IEEE Trans. Ultrason. Ferroelectr. Freq. Control 49 (9) (2002) 1245–1253, http://dx.doi.org/10.1109/TUFFC.2002.1041541.
[42] E.M. Viggen, H.K. Arnestad, Inhomogeneous P- and S-wavefields radiated into isotropic elastic solids, in: Proceedings of the 45th Scandinavian Symposium on Physical Acoustics, Norwegian Physical Society, Online, 2022, p. 13.
[43] R. van Kuijk, S. Zeroug, B. Froelich, M. Allouche, S. Bose, D. Miller, J.-L. le Calvez, V. Schoepf, A. Pagnin, A novel ultrasonic cased-hole imager for enhanced cement evaluation, in: International Petroleum Technology Conference, 2005, p. 14, http://dx.doi.org/10.2523/IPTC-10546-MS.
[44] S. Zeroug, S. Bose, Ultrasonic cement evaluation with the flexural wave imager: A new workflow to estimate cement wavespeeds, in: SPE Annual Technical Conference and Exhibition, Society of Petroleum Engineers, 2018, p. 12, http://dx.doi.org/10.2118/191675-MS.